NOVA SCHOOL OF SCIENCE & TECHNOLOGY

DEPARTMENT OF ELECTRICAL AND COMPUTER ENGINEERING

SIMÃO PEDRO RODRIGUES DA SILVA BRANDÃO VENDEIRINHO

BSc in Electrical and Computer Engineering

VEGETATION CHANGE DETECTION USING SYNTHETIC APERTURE RADAR IMAGES

MONITORING FUEL BREAKS THROUGH SAR IMAGING WITH SENTINEL-1

MASTER IN ELECTRICAL AND COMPUTER ENGINEERING

NOVA University Lisbon
November, 2024

NOVA SCHOOL OF SCIENCE & TECHNOLOGY

DEPARTMENT OF ELECTRICAL AND COMPUTER ENGINEERING

VEGETATION CHANGE DETECTION USING SYNTHETIC APERTURE RADAR IMAGES

MONITORING FUEL BREAKS THROUGH SAR IMAGING WITH SENTINEL-1

SIMÃO PEDRO RODRIGUES DA SILVA BRANDÃO VENDEIRINHO

BSc in Electrical and Computer Engineering

Adviser: André Teixeira Bento Damas Mora
Assistant Professor, NOVA School of Science and Technology

Co-adviser: João Pires
Researcher, UNINOVA

Examination Committee

Chair: Nuno Filipe Silva Veríssimo Paulino
Associate Professor with Habilitation, NOVA School of Science and Technology

Rapporteur: Filipe de Carvalho Moutinho
Assistant Professor, NOVA School of Science and Technology

Adviser: André Teixeira Bento Damas Mora
Assistant Professor, NOVA School of Science and Technology

MASTER IN ELECTRICAL AND COMPUTER ENGINEERING

NOVA University Lisbon
November, 2024

Vegetation Change Detection using Synthetic Aperture Radar Images
Monitoring Fuel Breaks through SAR Imaging with Sentinel-1

This document was created with the (pdf/Xe/Lua)LaTeX processor and the NOVAthesis template (v7.1.18) [1].

To my guiding star.

Acknowledgements

Before all, I would like to express my deepest gratitude to Professor André Damas Mora for believing, supporting, and guiding me when all paths seemed to lead to closed doors and giving up was the easiest thing to do. I also would like to thank my co-adviser, João Pires, for accompanying me throughout the more specific and technical aspects with his insight and expertise on the topic.

To my friends, who transformed the overwhelming pressure and stress of academic life into an unforgettable journey, I give you my token of respect and appreciation for all the moments we shared.

Lastly, to my family, my heartfelt thanks. All I am is nothing but a reflection of the values and love you've given me, and for that, I will be forever thankful for having you in my life.

”

“Of all things visible, the highest is the heaven of the fixed stars.”

— Nicolaus Copernicus, De revolutionibus orbium coelestium
(Astronomer and mathematician)

Abstract

In Portugal, a fuel break network is a crucial element for the control and suppression of forest fires. When maintenance work is done, by removing vegetation within a designated area, there is a need to monitor and evaluate its effectiveness. The implementation of fuel breaks spans large areas and to replace field monitoring, remote sensing applications based on optical satellite imagery have been developed. To combat the limitations of optical visibility in adverse atmospheric conditions, literature has shown Synthetic Aperture Radar (SAR) images are a viable solution and can serve as an addition to solidifying the existing monitoring applications.

The proposed solution is a processing methodology for Sentinel-1 SAR imagery to detect the removal of vegetation inside the designated area of a fuel break, this can be achieved by using existing SAR processing techniques and aided by a classifier created with machine learning. As a result, the developed methodology will deliver consistent monitoring data from fuel breaks which can be used to further reinforce existing optical-based solutions.

Keywords: Synthetic Aperture Radar, Sentinel-1, Remote Sensing, Change Detection, Fuel Breaks, Fires, Forests

Resumo

Em Portugal, a rede de faixas de gestão de combustível é um elemento fundamental para o controlo e a supressão dos incêndios florestais. Quando são efectuados trabalhos de manutenção, através da remoção de vegetação dentro de uma área designada, é necessário monitorizar e avaliar a sua eficácia. A implementação de faixas de gestão de combustível abrange grandes áreas e, para substituir a monitorização no terreno, foram desenvolvidas aplicações de deteção remota baseadas em imagens ópticas de satélite. Para combater as limitações da visibilidade ótica em condições atmosféricas adversas, a literatura tem demonstrado que as imagens de Radar de Abertura Sintética (SAR) são uma solução viável e podem servir como complemento para fortalecer as aplicações de monitorização existentes.

A solução proposta é uma metodologia de processamento de imagens SAR Sentinel-1 para detetar a remoção de vegetação dentro da área designada de uma quebra de combustível, o que pode ser conseguido utilizando técnicas de processamento SAR existentes e auxiliado por um classificador criado com *machine learning*. Como resultado, a metodologia desenvolvida fornecerá dados consistentes de monitorização das quebras de combustível que podem ser utilizados para reforçar as soluções ópticas existentes.

Palavras-chave: Radar de Abertura Sintética, Sentinel-1, Deteção Remota, Deteção de Alterações, Faixas de Gestão de Combustível, Fogos, Florestas

Contents

List of Figures

List of Tables

Acronyms

CART Classification and Regression Trees
CNN Convolutional Neural Network
CSV Comma-Separated Values

DEM Digital Elevation Models

EW Extra Wide swath

FB Fuel Break
FBN Fuel Break Network

GEE Google Earth Engine
GIS Geographic Information System
GRD Ground Range Detected

InSAR Interferometric SAR
IW Interferometric Wide swath

RADAR Radio Detection and Ranging
RGB Red Green Blue
RTC Radiometric Terrain Correction

SAR Synthetic Aperture Radar
SLAR Side-Looking Airborne RADAR
SLC Single Look Complex
SM Stripmap

WV Wave

1 Introduction

Forest fires have intensified over the past decades due to climate change which has created conditions that make these fires more frequent and difficult to control. As a result, there has been an increase in damage to human lives and entire ecosystems, not to mention the consequences of converting healthy biomass into more carbon dioxide in the atmosphere.

1.1 Motivation

It is of utmost importance to take proactive actions to prevent such fires and also to mitigate the damage caused by them. One such proactive action would be the creation of a Fuel Break Network (FBN).

1.1.1 Fuel Break

A Fuel Break (FB) is defined as an area where the tree cover and ground cover must comply with certain standards. These standards include the removal of vegetation at ground level and spacing between trees. Figure 1.1 illustrates a FB bisected along its symmetry axis (dotted line), highlighting the rules established by [2] regarding vegetative cover. Specifically, a road with a width of 5 meters should have no vegetation within the adjacent 10 meters, followed by strict regulations on tree spacing and ground clearance.

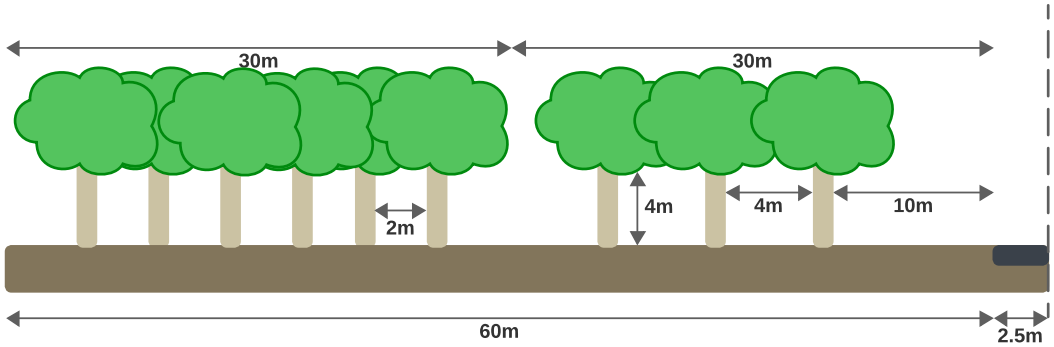

Figure 1.1: Fuel Break diagram

FBs are usually implemented in strategic locations that use the terrain's topology to their advantage, allowing cost reduction in their implementation and maintenance. The objective of a FB is to facilitate firefighting, prevent the spread of fire across regions, and consequently reduce the total affected area and the damage caused by the fire.

Performing regular maintenance work on the FBs, usually every two years, is a requirement as vegetation will regrow, replacing the vegetation removed with the previous maintenance work. In-person verification of compliance with the standards and effectiveness of the FBs becomes a time-consuming and arduous task given the total area that needs to be checked, not only for a single firebreak but also due to the need to perform this same task for multiple FBs. It would be advantageous to have a remote and more efficient methodology for verifying the conditions of the FBs.

To aid the creation of a FBN it is imperative to have a monitoring methodology capable of detecting changes that can guarantee the effectiveness of the implemented FBN. This is where Synthetic Aperture Radar (SAR) imagery comes in as a potential solution to monitor fuel load removal remotely. Besides healthy vegetation, fuel load also includes decaying vegetation, litter, and any type of combustible matter found in the region.

1.1.2 Remote Sensing

Remote sensing is the process of observing and analyzing the Earth's surface and atmosphere, making it ideal for monitoring large areas with difficult access points like FBs. Data is collected from a distance, typically via satellites or aircraft, allowing for the monitoring of environmental changes, resource management, and disaster response. This technology employs various sensors capable of gathering relevant data, which can be processed and analyzed to understand different phenomena on Earth.

Among the multiple remote sensing techniques, SAR stands out for its unique capabilities.

1.1.3 Synthetic Aperture Radar Imagery

SAR, as the name implies, is a form of radar that is used to create detailed images of landscapes, irrespective of atmospheric weather conditions or time of day [3]. Unlike traditional optical imagery that relies on passive sensors to capture visible light, SAR uses an active sensor that transmits microwave signals towards the Earth and measures the signals that are reflected. The ability to penetrate clouds and operate effectively with low light conditions makes SAR exceptionally valuable in many applications.

SAR imagery is a powerful tool with unique capabilities which makes it a great candidate to aid the task of monitoring FBs. By analyzing SAR imagery, it is possible to detect changes in vegetation density and structure, identify areas where vegetation has regrown [4][5], and assess the overall condition of the FBs. Combining SAR data with information gathered by other remote sensing technologies can provide a comprehensive understanding of the FBs' status and help prioritize maintenance efforts.

1.2 Objectives

The use of SAR imagery for monitoring and maintaining FBs presents itself as a promising solution to the challenges associated with manual inspections and optical-based remote sensing applications such as the ones developed in [6][7].

The work that follows aims to create an image processing methodology for SAR imagery provided by the satellite Sentinel-1A of the Copernicus Sentinel-1 mission to detect changes within a designated FB area with the ultimate goal of enhancing and aiding current monitoring methods, thereby contributing to better forest fire prevention and control.

1.3 Document Structure

In this introductory chapter, a brief context was provided to explain the relevance of this work, including its motivation and objectives. The second chapter will aim to provide a technical explanation of the inner workings of SAR, processing techniques for this type of data, and its current applications. The third chapter will explain the proposed solution to achieve the end goals established for this work. Relevant evaluation metrics as well as a sample of the obtained results from the developed methodology will be shown in the fourth chapter. Finally, the last chapter will be a short conclusion about the developed work, providing some final insights on the produced results, possible improvements, and future integration to help forest fire prevention.

2

State of the Art

This chapter will provide a more technical explanation of the inner workings of SAR, processing techniques, present its current applications that can be considered relevant to this work, and lastly a brief mention to relevant software in SAR image processing.

2.1 Fundamentals of Synthetic Aperture Radar

SAR remote sensing is based on Radio Detection and Ranging (RADAR) which is a type of active sensor capable of transmitting microwaves and measuring the reflected signal of the target location. Being based on RADAR, this technology proves itself reliable in regions with adverse atmospheric conditions and in darkness. SAR was created as an evolution of Side-Looking Airborne RADAR (SLAR) airborne systems to improve image resolution problems.

2.1.1 Airborne Radar Imaging

Creating images with SLAR systems can be challenging. Image resolution is of utmost importance for detailed feature analysis and this resolution is correlated to the antenna footprint, in other words, one pixel of the image is the area instantaneously illuminated by the signal of the antenna. This footprint is directly correlated with the antenna's beamwidth and the distance to its target. This is shown in equation 2.1 where the antenna's footprint size S can be approximated as the beamwidth β (wavelength λ divided by the length L of the antenna) multiplied by the distance R to the targeted area on the ground [8].

$$S \approx \frac{\lambda}{L} R = \beta R \tag{2.1}$$

It is important to note that equation 2.1 is generalized and can be applied for both range and azimuth. For a better understanding, Figure 2.1 is given as an example where the azimuth footprint can be calculated with the known values of orbit height H, beamwidth β, and look angle θ. We can rewrite equation 2.1.

$$S \approx \beta \frac{H}{\sin \theta} \tag{2.2}$$

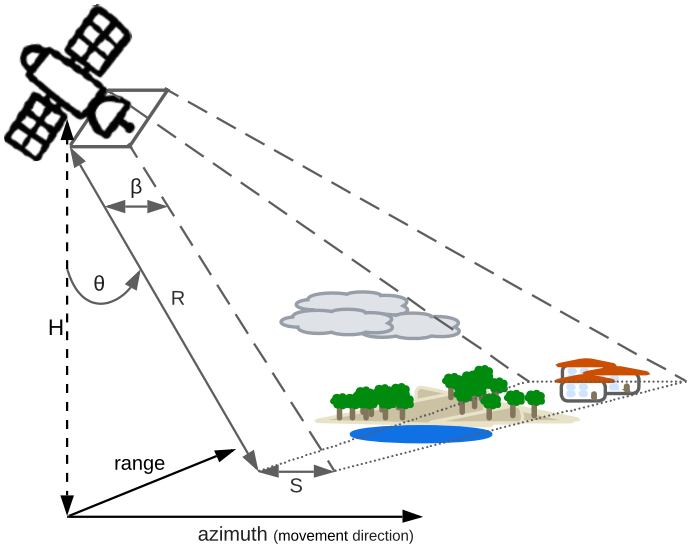

Figure 2.1: SLAR azimuth footprint equation diagram.

A resolution problem arises with SLAR. If we consider the average orbital altitude of a satellite to be 700km [9], with an azimuth look angle of 30 degrees, 5cm wavelength, and the antenna's length of 5m, the azimuth resolution would be 14km which by itself is unusable for precise earth monitoring applications. For obvious reasons orbit height can't be changed, for a given region the look angle is dependent on the orbit path so it can't be changed as well, wavelength is inherent to the type of sensor we're using and also cannot be changed leaving the length of the antenna, also called as aperture, the only viable parameter to be fine-tuned for higher resolutions.

In the previous example with an aperture of 5 meters, a resolution of 14 kilometers was achieved. Scaling antenna size is also highly impractical especially when sending it into orbit. This is where synthetic aperture comes into play.

By taking multiple acquisitions between two points in space and combining them into a single image the antenna's size is being scaled up synthetically to the size of the distance between these two points. Discovered by Carl A. Wiley in 1952 [10], this technique has been used ever since to create RADAR images with very high resolutions.

As of today, SAR can achieve spatial resolutions ranging from 100m to as little as sub 1m resolutions [11][12][13].

2.1.2 Signal Wavelength

The microwave wavelengths used by SAR imaging systems have a huge impact on the type of end product received and are the first factor to consider when creating an application that relies on RADAR. Different wavelengths have different penetration properties, therefore, must be used according to specific application scenarios as seen in Table 2.1 adapted from [14].

Table 2.1: SAR applications based on wavelength

Bands	K-Band	X-Band	C-Band	S-Band	L-Band	P-Band
Wavelength (cm)	0.75 - 2.4	2.4 - 3.75	3.75 - 7.5	7.5 - 15	15 - 30	30 - 100
Mapping/Monitoring						
Canopy	x	x				
Flooded Grass	x	x	x			
Flooded Canopy					x	x
Flood	x	x	x	x	x	x
Earth Surface	x	x	x	x	x	x
Soil Moisture	x	x	x	x	x	x
Penetration						
Canopy (Low/Medium)			x	x		
Canopy (High)					x	x
Precipitation			x	x	x	x
Cloud, Dust, Smog		x	x	x	x	x

As mentioned in section 1.1.3, SAR enables the monitoring of Earth's surface in all weather conditions during day or nighttime as a result of the properties of the signal used by its sensor.

2.1.3 Signal Polarization

Signal polarization refers to the orientation of the electric field of a signal when transmitted or received. SAR utilizes horizontal and vertical polarization in its signals. The polarization of the transmitted and received signals is commonly labeled with two letters: the first letter indicates the transmission polarization, and the second letter indicates the received signal polarization. For example, a signal that is vertically polarized on transmission and horizontally polarized on reception is labeled as VH-polarization. The common signal polarization used in SAR the following [15]:

- VV — vertical transmission ; vertical reception
- VH — vertical transmission ; horizontal reception
- HV — horizontal transmission ; vertical reception
- HH — horizontal transmission ; horizontal reception

Polarimetry plays a crucial role in monitoring and classification applications. The strength of the signal reflection combined with signal polarization can provide useful information to classify the type of surface the sensor is observing, such as water bodies,

forests, urban areas, crops, or bare soil [16]. When used in time series analysis, it can serve as the basis for change detection methods. The following image is an example of a SAR VV image.

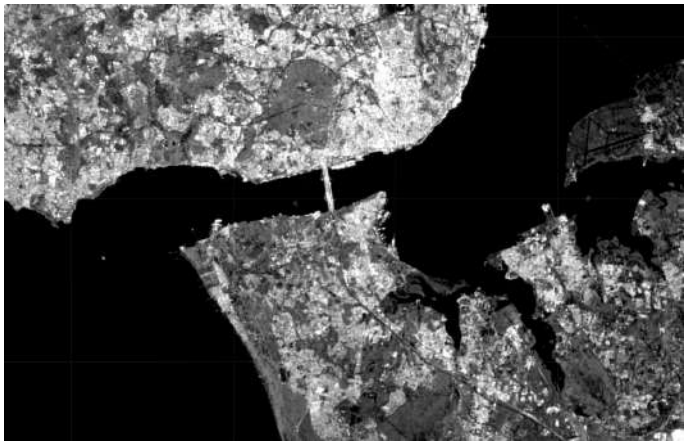

Figure 2.2: Example of a monthly mean SAR VV image taken over Lisbon and created with Sentinel-1 GRD products.

2.1.4 Scattering Types

Signal scattering refers to the type of reflection that occurs when a signal collides with a surface. There are three main types of scattering, as illustrated in Figure 2.3.

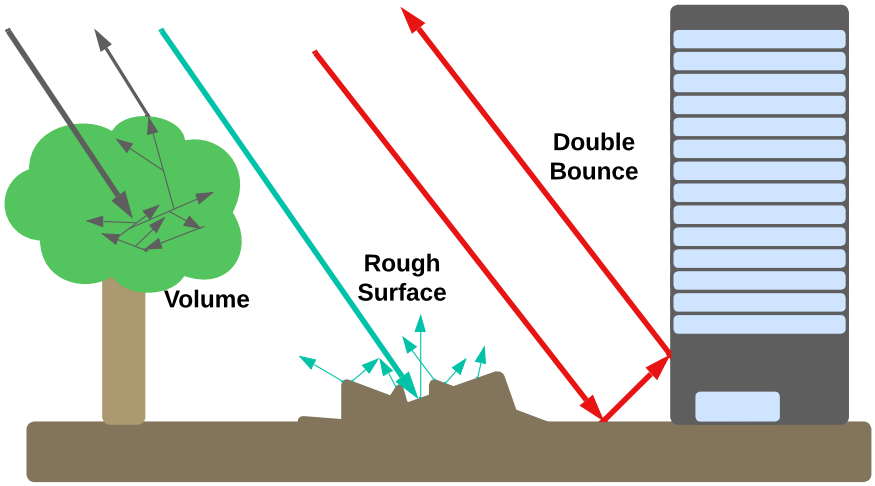

Figure 2.3: Three main types of scattering: Volume, Rough Surface and Double Bounce adapted from [8].

- Volume scattering occurs when the signal is directed toward a penetrable surface.
- Rough surface scattering occurs when the signal encounters angular surfaces.
- Double bounce scattering occurs when there are smooth surfaces that reflect the transmitted signal very well.

These are the main types of scattering, and combinations of them can help classify a wide range of elements found on Earth's surface, such as different types of bare soil, vegetation, water, and urban regions. Scattering is the main mechanism that enables polarimetric classification due to its effect on signal power and polarization when received by the SAR sensor [17].

Moisture has a significant impact on signal power. The backscattered signal is not only dependent on surface geometry and density, where the signal can or cannot penetrate but also on the moisture content, which can affect the dielectric properties of the surface. This, in turn, impacts how much of the signal is reflected and how much is absorbed. There is evidence that soil moisture can induce changes in signal power exceeding 15 dB [18].

Moisture affects all SAR bands. This can become problematic when classifying different types of land cover, as the penetration depth δ_p varies with moisture levels, affecting the dielectric constant (composed of a real component ϵ_r' and an imaginary component ϵ_r'') of the target medium, as shown in equation 2.3 and Figure 2.4 [8].

$$\delta_p \approx \lambda \frac{\sqrt{\epsilon_r'}}{2\pi\epsilon_r''} \tag{2.3}$$

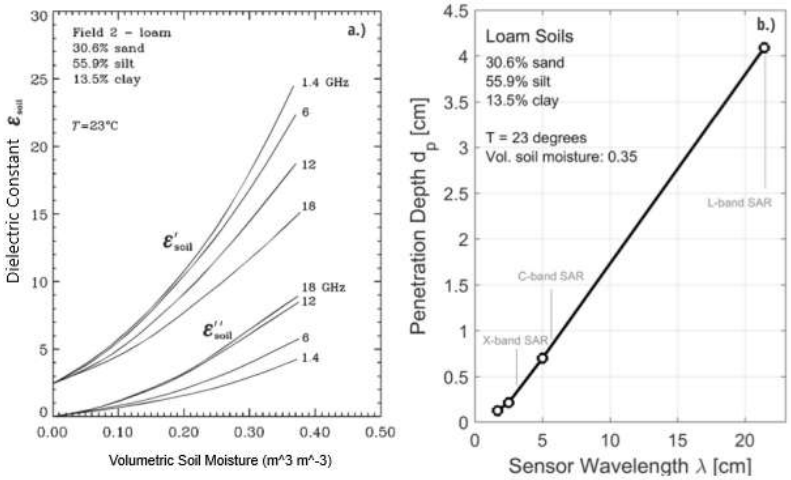

Figure 2.4: a) Relationship between soil moisture and dielectric constant; b) Dependence of penetration depth on the sensor wavelength for a fixed soil moisture. Graphs sourced from [8].

Figure 2.4 extends the previous equation, with the graph on the left demonstrating how the dielectric constant changes with different levels of soil moisture for various SAR bands. The graph on the right shows the depth of penetration achievable with a fixed moisture level of 0.35, indicating that bands with longer wavelengths have higher penetrative capabilities compared to those with shorter wavelengths.

2.1.5 Inherent Noise and Geometry Problems

Despite being effective in adverse atmospheric conditions, SAR has its drawbacks placed on the surface geometry and in its sensor. SAR needs to convert an analog signal into a digital signal to create an image. Thermal and quantization noise can be introduced in the images by the sensor's electric circuit; however, this type of noise is not the real issue. Speckle noise is the real problem and it is caused by the reflection of out-of-phase signals. This type of noise has very peculiar characteristics such as being a granular multiplicative noise and depending on location it can vary, making it very difficult to remove with normal filtering techniques [19][20].

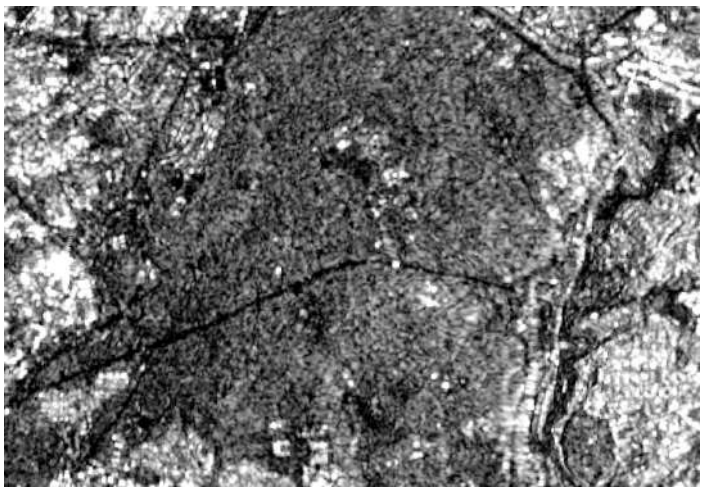

Figure 2.5: SAR image with speckle noise and geometric distortion.

Speckle noise is not the only problem, terrain topography as barely seen in Figure 2.5 is also one. As mentioned earlier a SAR sensor directs its signal at a certain angle towards the ground and with Earth's surface not being a smooth flat surface, geometry problems start to appear. As mentioned in [8], foreshortening, layover, and shadowing are the three main causes of geometric distortion in SAR images. In mountainous regions, when the sensor is facing a slope and depending on the slope angle the imaged face of the slope can be seen as compressed (foreshortening) or if the reflection from the base of the slope overlaps with the reflection from the slope itself then two different regions will be mapped as being the same location (layover). The last geometric problem in SAR is the shadowing effect where the look angle is not enough to reach areas obstructed by features such as a steep mountain face as seen in Figure 2.6. These geometry problems do not have a straightforward solution since foreshortening and layover can be reduced by increasing the look angle, but shadowing effects will worsen and vice-versa [8].

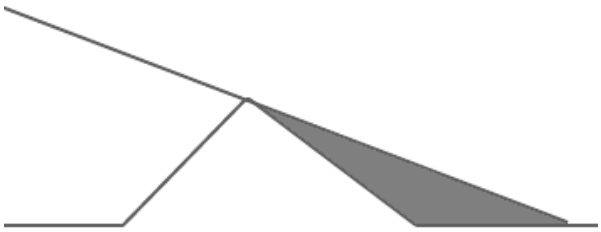

Figure 2.6: Diagram example of shadowing where the SAR sensor cannot gather any data from ground surfaces enveloped by the grayed-out zone, adapted from [8].

2.2 Image Acquisition and Processing

In this section it will be explained how the satellite Sentinel-1 acquires its SAR images as well as a set of relevant SAR processing techniques.

2.2.1 Acquisition Modes

Creating SAR images involves more than just pointing a RADAR towards Earth and displaying the results. For the Copernicus Sentinel-1 C-band SAR instruments, there are four modes of data acquisition: Stripmap (SM), Interferometric Wide swath (IW), Extra Wide swath (EW), and Wave (WV).

These modes provide different spatial resolutions and cover different total ground areas, called swaths. In Portugal, Sentinel-1 uses the IW mode to create 250 km swaths with incidence angles ranging from 29.1 to 46.0 degrees. The available products targeting Portugal's continental territory are made with signals of VV and VH types and include the amplitude of the signal as well as the incidence angle for each pixel [12][21].

Sentinel-1 SAR products are available to be accessed and downloaded using the Copernicus Browser platform, or in some cases, specific products may be available on platforms such as Google Earth Engine.

2.2.2 Processing Techniques

SAR has different levels of products ranging from raw data to processed and ready-to-use images. Sentinel-1 products range from level 0 to level 2 and each level adds more preprocessing to the images. The products from Sentinel-1 are presented like this [12]:

- Level 0 products consist of compressed, unprocessed instrument source packets, including annotations and auxiliary information necessary for further processing. These products are the foundation for all higher-level SAR products. Their compression allocates more bits to bright scatterers. To be usable, Level-0 data must be decompressed and processed with focusing software.

- Level-1 products are the primary data products for most users, serving as the basis for higher-level products. These products are divided into Single Look Complex (SLC) and Ground Range Detected (GRD). SAR parameters are periodically updated to maintain scene homogeneity and each product is georeferenced, time-tagged, and corrected for azimuth bi-static bias to ensure accuracy in georeferencing.
- Level-2 products are derived from Level-1. These products are used for wind, wave, and current applications.

Level-1 SLC and GRD products are commonly processed with the following techniques on a wide range of applications.

2.2.2.1 Speckle Noise Filtering

Speckle noise filters are essential for any type of application involving SAR, hence the existence of multiple implementations all with the aim of speckle noise reduction. Some of the most popular filters are the Lee filter, the Refined Lee filter, the Boxcar filter, filters based on multi-temporal stacking and non-local means filters [8][22][23][24]. Different filters yield different results. For example, using the Boxcar filter can result in the loss of important edge information, as it is primarily used in homogeneous areas. In contrast, the Refined Lee filter, with its calculations of local pixel directional mean and variance values, helps preserve features with clearly defined edges.

2.2.2.2 Radiometric Terrain Correction

Radiometric Terrain Correction (RTC) involves adjusting the SAR data to remove distortions caused by topographic variations, ensuring the reflected signal's values are accurate for each pixel. This is crucial for reliable data interpretation, especially in areas with significant elevation changes, as uncorrected data can lead to errors in applications like land cover classification and biomass estimation [25].

In RTC there is a challenge consisting of modeling the interaction between the SAR signal and the terrain with accuracy. This requires detailed Digital Elevation Models (DEM)s and precise knowledge of the SAR imaging geometry. The correction process needs to account for factors such as the local incidence angle, surface roughness, and the presence of vegetation, which can all affect the backscattered signal. Other factors such as soil moisture can bring the necessity of sophisticated algorithms and computational techniques to achieve an accurate correction [25].

As an example, Sentinel-1 Level-0 products (raw data) need to be processed with RTC to become Level-1 SLC and GRD products [12].

2.2.2.3 Interferometric SAR

Interferometric SAR (InSAR) differs from polarimetric and signal amplitude analysis. There are two types of InSAR: single-pass and differential. Both single-pass and differential

InSAR focus on analyzing the signal's phase between two different images, with the main goal of mapping terrain topography and detecting changes.

In single-pass InSAR, as the name implies, the acquisition of the two images is done on the same date. This can be achieved by using two displaced antennas, each capturing an image simultaneously, or by using the same antenna to capture two images at different moments during its passage over the target area [26]. Single-pass InSAR enables topographic applications such as measuring forest height and mapping vegetation.

Differential InSAR utilizes the difference in the signal phase between acquisitions from different dates. With differential InSAR, the signal's phase is particularly affected by displacement considering terrain topography can be compensated for or eliminated to get the final interferogram (InSAR product image). This resulting image usually displays a gradient correlated with movement distance, where terrain altitude and lateral movement can be seen [27]. An example of a differential InSAR interferogram is given in Figure 2.7.

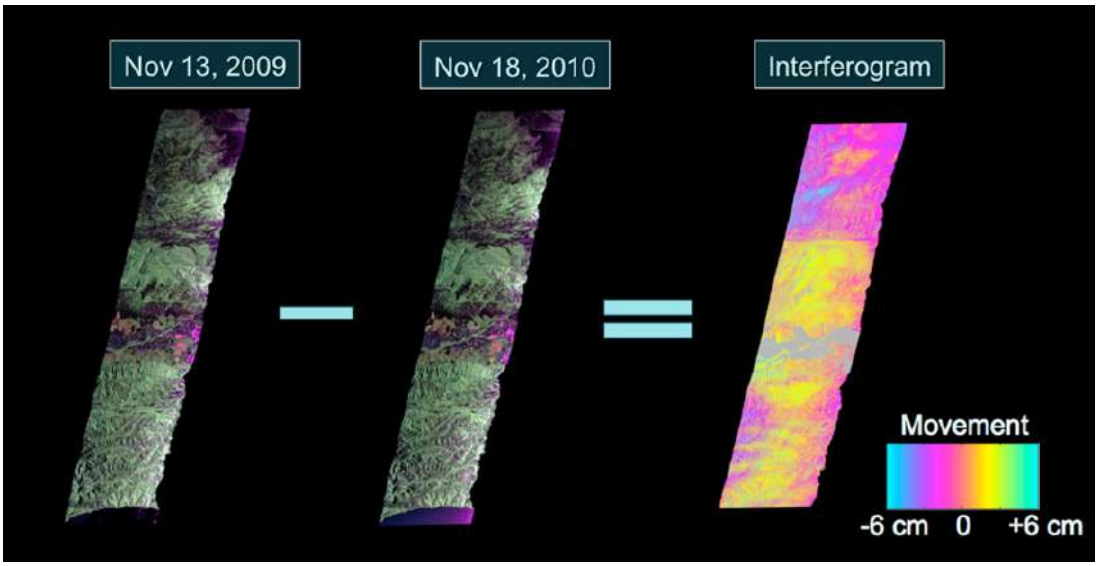

Figure 2.7: Interferogram of San Andreas Fault in California. Credit: NASA/JPL-Caltech, sourced from [27].

2.2.2.4 Polarimetric SAR - Composite Images

Composite images, created by combining multiple images, can be categorized into two types.

The first type is temporal composites. These are created by assigning the Red Green Blue (RGB) channels of a normal image to signals from three separate acquisition times, using color to express changes over a designated period. Temporal composites can also refer to the average or mean image generated from multiple images spanning a period of time, typically a month or a season.

The second type uses multiple images with different polarization from a single point in time, inserting them into the RGB channels of a normal image. This type of composite is useful for distinguishing certain terrain characteristics and visualizing different types of land cover.

In Figure 2.8 on the left image we can see how the crops on the Tagus River marshlands change over time with a VV stack composite. Each RGB channel is occupied by a VV polarized image taken on different dates therefore change is given by the display of color while unaltered regions remain on a gray scale. The image on the right is an RGB composite created with VV VH and VV/VH as sources for the respective RGB channels and it is possible to distinguish urban areas with very bright colors (high-intensity backscattering), vegetation zones in shades of green and the zones in black and darker colors representing low-intensity backscattering zones such as water.

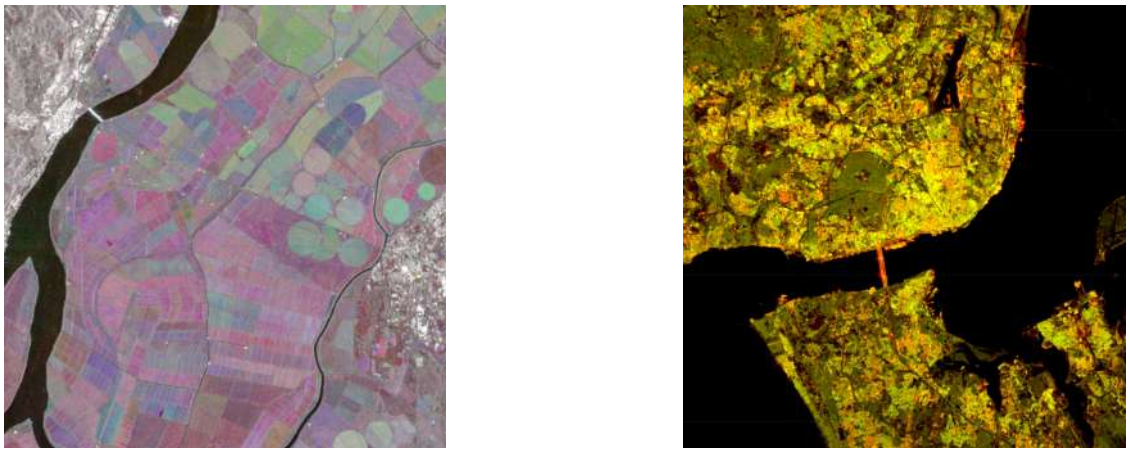

(a) VV Stack.

(b) RGB - R:VV G:VH B:VV/VH.

Figure 2.8: VV stack(a) and RGB(b) SAR composites.

2.2.2.5 Machine Learning for SAR

Land cover classification is one of the most studied subjects when it comes to SAR use cases. As with any other classification problem, the incorporation of machine learning techniques has become a staple.

Supervised learning is the most common practice as done in [16] or [28] for example. In this method of training, algorithms such as Support Vector Machines, Random Forests, and Neural Networks are trained using labeled datasets. The classifier learns the relationship between SAR signal patterns and specific land cover types. Once trained, the model can classify new SAR data with high accuracy. For example, Random Forests, which consist of multiple decision trees, have been effective in classifying complex land cover types due to their ability to handle large datasets and multiple variables.

Unsupervised training can also be achieved by using clustering methods on the dataset to remove the data labeling process required in supervised learning [29].

The final method of machine learning is deep learning where a Convolutional Neural Network (CNN) is created and fine-tuned for the application. Deep learning can automatically extract hierarchical features from raw SAR imagery, enabling the identification of complex patterns and structures. Deep learning models require extensive training data but offer superior performance when compared to traditional supervised learning [30].

2.2.2.6 Change Detection

In [31], a methodology for change detection is proposed by predicting SAR images through a CNN based on the U-net architecture [32]. The neural network is trained with a set of SAR images from different dates, their respective acquisition parameters from when they were taken, and a DEM. The input for the CNN is the set of parameters from the real image and the output is a predicted image. After predicting the image, a difference image can be created. Three methods were proposed to choose the parameters for the two images used in the creation of the difference image:

1. Use the images with the closest incidence angle and the same orbit direction.
2. Use the images with the closest time gap and the same orbit direction.
3. Use the images with the closest time gap.

After creating the difference image, the authors use two classification methods to compare it to normal difference image creation. This methodology proved itself as an improvement over the normal difference image creation methods.

Figure 2.9 represents the methodology created in [31].

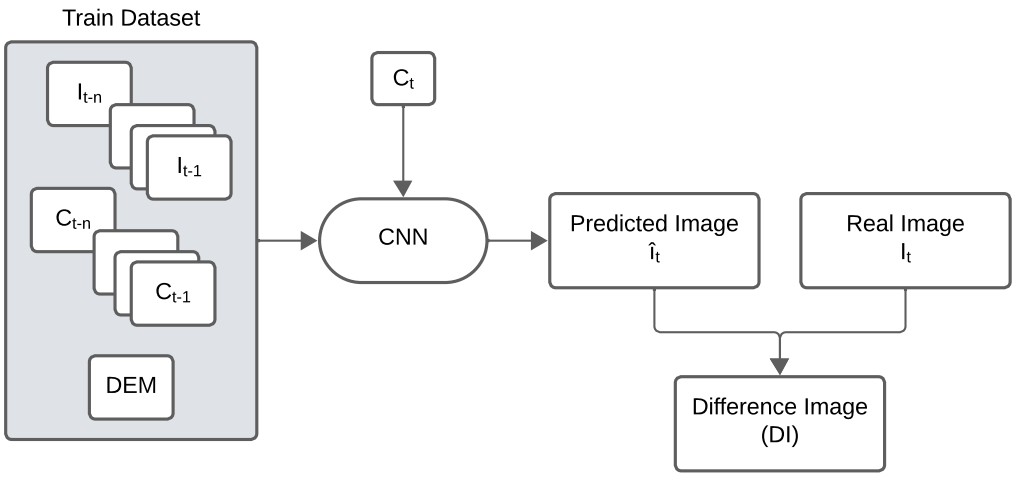

Figure 2.9: Methodology for difference image creation adapted from [31].

Despite the good results, it is important to note that the classification methods used for the difference image were not the most advanced ones thus not ruling out normal methods for difference image creation.

Difference image creation can be simplified and accomplished with two processed images to reduce speckle noise, leaving the complexity for the change detection algorithm. A novel solution for detecting change in difference images is given by [33]. In this approach, a Convolutional-Wavelet Neural Network is used for detecting changes using regions extracted from salient regions in the difference image.

Figure 2.10 shows the mentioned approach. The first step in this methodology is to reduce the speckle noise in both images and create a difference image with a log-ratio operator. In the resulting difference image, salient regions are regions with high contrast. Each pixel is compared to every other pixel in the image with the absolute value of their difference, resulting in enhanced salient regions. A classification threshold is applied and then the neural network is used to produce a change map.

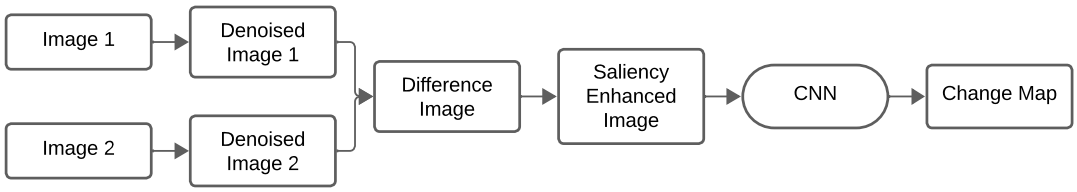

Figure 2.10: Methodology for change detection based on CNN with saliency enhancement adapted from [33].

Clustering can also be used to aid in change detection. The methodology from [34] shown in Figure 2.11 demonstrates how a popular clustering method, Fuzzy C-Means, can be used as an input parameter to create a change map.

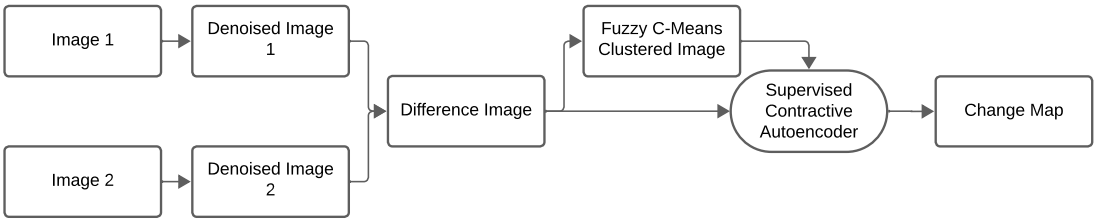

Figure 2.11: Methodology for change detection aided with clustering adapted from [34].

This methodology differs from the others also in the processing tool used to build the change map. In [34], a Supervised Contractive Autoencoder is used as the deep learning model to receive both the clustered image and the difference image as inputs to create the change map.

The two previous methodologies follow the normal process of change detection. Typically, this process can be divided into three distinct phases.

1. The input images (Level-0 or Level-1 products) are preprocessed to correct geometry and speckle noise.

2. The preprocessed images are used to create difference images using an equation of choice. The following equations are examples of how difference images (DI) can be created[31][35][36]. Here, x and y are the pixel coordinates, and the band (b) indicates the used signal polarization:

   - **Subtraction** — $DI(x, y, b) = I_1(x, y, b) - I_2(x, y, b)$
   - **Absolute Difference** — $DI(x, y, b) = |I_1(x, y, b) - I_2(x, y, b)|$
   - **Log-Ratio** — $DI(x, y, b) = |\log(\frac{I_1(x,y,b)}{I_2(x,y,b)})|$
   - **Band Distance** — $DI(x, y) = \sqrt{\sum_b (I_1(x, y, b) - I_2(x, y, b))^2}$

3. The difference image is used as input (with or without relevant correlated data) for a classifier, resulting in the output of a change map.

2.3 SAR Applications

SAR enables a vast range of monitoring applications including agriculture, forestry, maritime surveillance, and natural disaster management just to name a few. All of these applications employ methods of temporal change analysis and land cover classification, most applications use both methods at the same time while in some cases only one of the methods can suffice.

As the name implies, temporal change analysis is the process of gathering data across a given period and making the appropriate comparisons between different points in time, with the aim of generating datasets that can be used for change detection purposes. Land cover classification is also simple to understand, it is the labeling of Earth's surface characteristics. It can be a very simple and generalized classification such as soil, water, and vegetation, or it can be very intricate and complex by creating sub-labels for types of soil, distinguishing bodies of water, or separating vegetation into different plant species and types of ecosystems.

Agriculture and forestry are the fields most relevant to the goal established for this work of monitoring and detecting changes in FBs. These fields involve the monitoring of different types of vegetative cover, including species of trees, shrubs, or tall grass. Human intervention in vegetation and phenology studies are the main areas of study in these fields.

The following sections will focus on a subset of SAR applications relevant to this work in agriculture and forestry.

2.3.1 Agriculture

SAR's impact on modern agriculture is undeniable and has enabled more efficient and sustainable farming practices.

Analyzing the backscatter signals of a crop field can aid in monitoring growth and estimating proper harvest time. A study case done for a rice crop field in Japan (Figure 2.12) has shown that Sentinel-1 SAR images are capable of monitoring rice crop growth by analyzing the VV and VH signals alongside the ratio obtained by the division of both signals (VV/VH) [37].

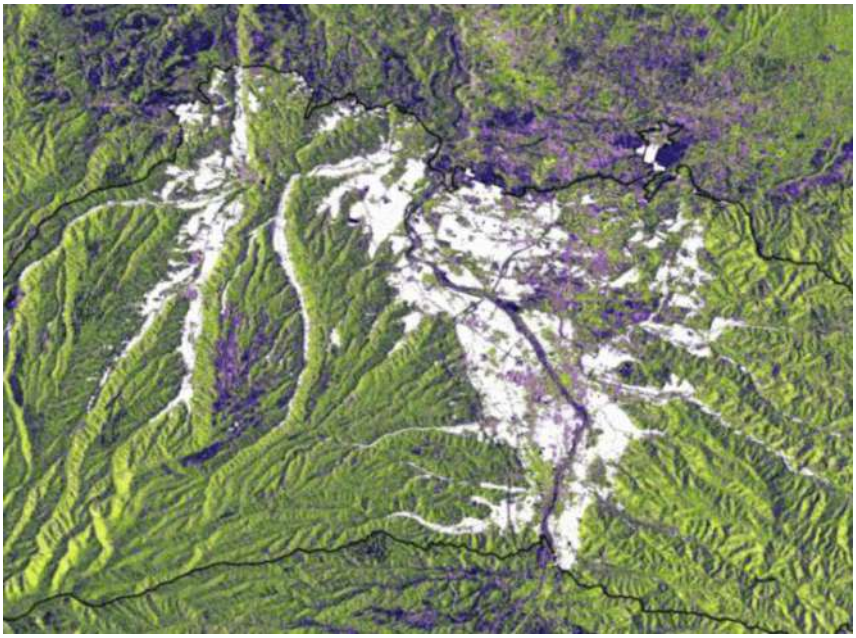

Figure 2.12: Mapped rice crops in white overlaid on a Sentinel-1 SAR color composite (R: VV, G: VH, B: VV/VH), sourced from [37].

Water management in agriculture has been an increasing point of concern in recent times. Soil moisture is a crucial factor for plant growth, and irrigation needs and is what determines farming yields. Soil moisture estimation can be achieved with SAR data by detecting changes in the dielectric properties of the soil, as its effect was mentioned in section **??**. The information given by SAR data can lead to better irrigation schedules and drought monitoring systems as stated in [38].

Land cover classification can also be applied in agriculture. Mapping crop types based on seasonality can improve resource allocation and give further insight into the role climate change is playing in agriculture. For better mapping precision SAR data can be used simultaneously with optical data as mentioned in [39], where Sentinel-1 data was used in conjunction with Sentinel-2 (the optical mission from Copernicus) to achieve such goal.

2.3.2 Forestry

Forestry monitoring applications also benefit from SAR providing information used for example in the detection of deforestation and forest mapping as well. This is explained with high detail in [40].

Illegal logging is a serious threat to biodiversity and contributes to climate change by reducing the number of trees that can absorb carbon dioxide. SAR can detect changes in forest cover by comparing backscatter signals from different times. These temporal changes in backscatter data can reveal areas where deforestation has occurred, allowing interventions if the deforestation is deemed as a cause of illegal activities. This aspect of time series analysis also brings the possibility of natural disaster monitoring. Events such as storms, forest fires, and floods can change forest topology. The perception of the damages caused can be aided with SAR by analyzing images from before and after the occurrence of these natural disaster events.

Figure 2.13 demonstrates a set of time series charts where the red curve corresponds to data from a VV polarized signal and the blue curve is linked to a VH polarized signal. In these charts changes in the terrain can be located in time by correlating them to abrupt changes or pattern disruptions.

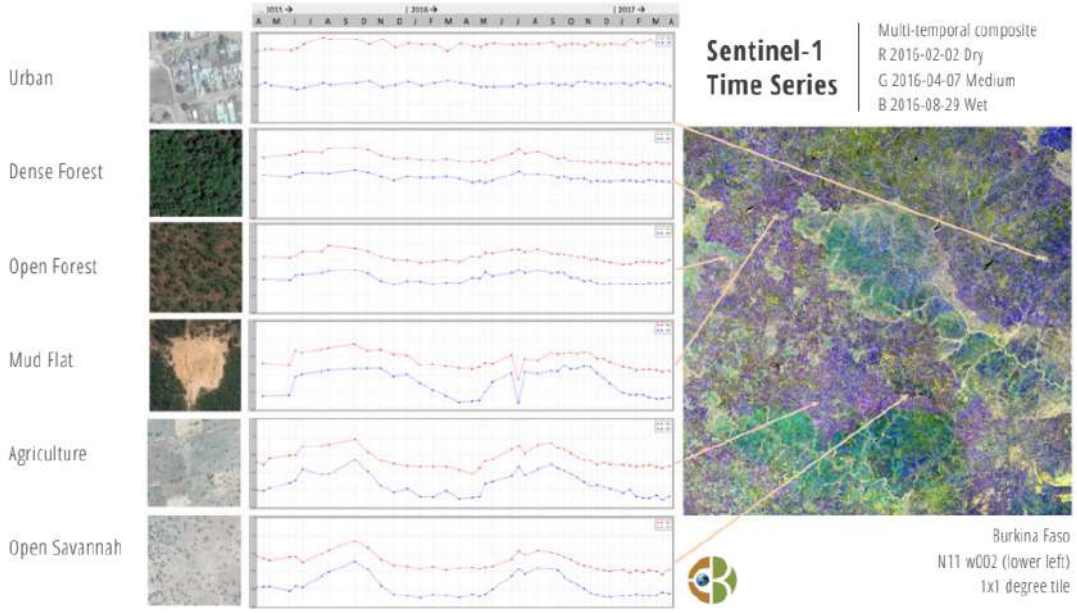

Figure 2.13: Sentinel-1 time series of different land cover types including forest biomes, sourced from [40].

Forest mapping is crucial for sustainable management, biodiversity conservation, and carbon stock assessment. SAR can map forest areas and classify different forest types, assess forest density, and monitor changes. This detailed mapping supports forest management by providing accurate data on forest cover and composition, essential for conservation planning and health assessment. SAR also estimates biomass by analyzing backscatter signals, aiding in monitoring carbon storage and emissions, which is vital for climate

change studies and environmental conservation.

2.4 Relevant Software for SAR Image Processing

SAR imagery requires specialized software to handle and process the large and complex datasets it produces. These tools are essential for applications such as land monitoring, disaster management, and environmental change detection. This section outlines some of the most relevant software for SAR image processing.

2.4.1 Sentinel-1 Toolbox

The Sentinel-1 Toolbox is a dedicated platform for processing SAR data from the European Space Agency's Sentinel-1 mission. It offers comprehensive tools for SAR image calibration, filtering, terrain correction, and geocoding. The software also supports advanced SAR applications such as interferometry, polarimetry, and time-series analysis, making it versatile for both research and operational uses.

2.4.2 Google Earth Engine

Google Earth Engine (GEE) is a cloud-based platform designed for large-scale environmental data analysis. While primarily known for optical satellite data, GEE also supports the Sentinel-1 SAR GRD dataset, providing these images with thermal noise removal and RTC processing already applied to them[41], in sum, the required processing for a GRD product. This platform can handle time-series data making it useful for applications such as land cover change detection, and monitoring deforestation. From being cloud-based, this platform has the ability to process vast amounts of data without requiring local storage or high computing power. It can be accessed through Application Programming Interfaces (APIs) in JavaScript and Python, allowing custom scripts for specific analysis tasks.

2.4.3 Geographic Information System Software

Geographic Information System (GIS) software is often used in the interpretation and visualization of geocoded data with powerful tools that allow users to overlay SAR imagery with other geospatial datasets, facilitating spatial analysis for applications like urban planning, disaster management, and environmental monitoring.

2.5 Overview

Some key elements for the methodology can be taken from the state of the art such as the necessity for RTC processing and speckle noise filtering, as well as the integration of machine learning in change detection classification and time series analysis to detect

abrupt changes. There is also a decision to be made regarding the technological platform for developing the methodology. GIS software and the Sentinel-1 Toolbox require local processing and storage, whereas GEE handles everything in the cloud.

3

Image Processing Methodology

The intention of this chapter is to explain the image processing methodology developed as the solution to the issue stated in Chapter 1. To achieve this goal, a detailed overview of how the methodology works will be provided, followed by the analysis of each individual processing step that comprises the proposed solution. It is also important to mention that image processing in this methodology was developed solely using the GEE platform with its integrated JavaScript code editor. This approach means that all processing steps and resource storage are handled in the cloud (Google's servers), and any device with access to an internet browser can interact with and obtain relevant data from this methodology.

The developed code for this methodology can be found on GitHub [42].

3.1 Methodology Overview

As explained in the previous chapter, SAR images require a vast amount of processing when used for real-world applications. For this reason, the methodology can be split into two distinct parts to facilitate understanding. In addition to improving clarity, splitting can also reduce computation times, which will be explained further ahead. The first part consists of image preprocessing steps, and the second part involves change detection processing, ultimately leading to the final products of the methodology.

As seen in Figure 3.1, image preprocessing requires access to base resources, such as a Sentinel-1 SAR GRD image collection and the geometry of a land feature, in this case, the geometry of a FB.

The first step is filtering the image collection to obtain only the images that contain the desired feature. The filtered images are cropped to match the geometry of the FB, improving computational efficiency and reducing storage requirements. The next step, slope correction, is important as it helps minimize layover and shadow artifacts that affect certain areas of the images[43][44]. After the RTC step, the image goes through speckle noise reduction using the Refined Lee Filter[24]. At this stage, the images can be grouped by month and combined into a single image, also known as a monthly temporal composite, using a median operator. Finally, each monthly image receives a new band with the ratio

value of the VV and VH bands.

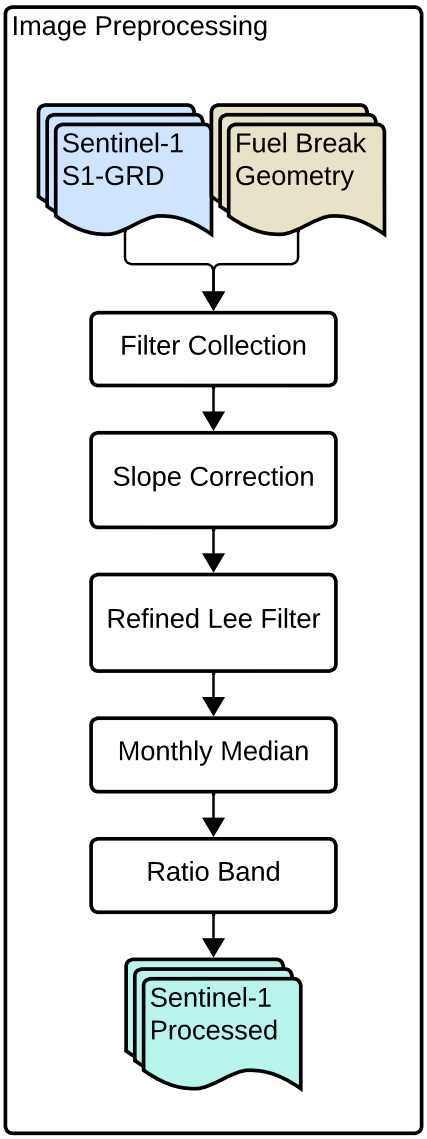

Figure 3.1: Preprocessing diagram of the methodology.

Preprocessing is computationally intensive, and if done on demand alongside the change detection processes, it would have caused a runtime error on Google's servers. Splitting the methodology was required for this specific reason.

Moving onto the change detection, just like in preprocessing, the two required resources are an image collection and the FB geometry. However, the image collection must be a Sentinel-1 GRD collection that has undergone preprocessing, and the FB geometry must be the same or be within the bounds of the geometry used in preprocessing. Figure 3.2 shows the workflow and steps required to achieve the methodology's final products.

The change detection process starts with the binary classification of each image from the processed Sentinel-1 collection. The classified images are then used to create change maps through a subtractive operation. At this stage, three datasets are available: the

processed SAR images, the binary classified images, and the binary change maps. Note that if N is the number of images in the binary collection, the change map collection will contain N-1 images.

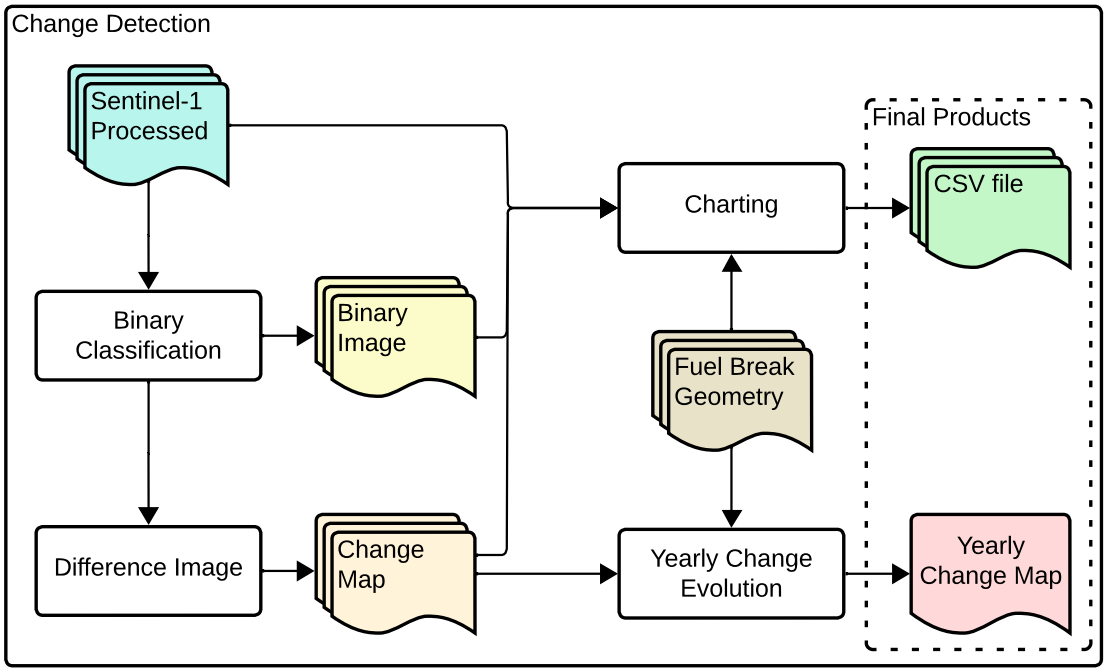

Figure 3.2: Change detection diagram of the methodology.

The final products of the change detection process are Comma-Separated Values (CSV) text files and an image depicting the yearly change map for the selected FB. SAR and binary images, along with the change maps, can be used to generate CSV text files with information within the FB geometry boundaries. In GEE, monthly charts, such as median band values, land cover area, or changed area, can be created and exported as CSV files. Time series analysis of the charts can reveal phenology trends in the FB and distinguish disruptions caused by maintenance work. The second final product, the yearly change map, compiles all the changes detected over a year into a single, easy-to-read image. Depending on how the compilation is done, the change map image may have different interpretations. The map will display the first occurrence of change, specifically from vegetation to bare ground, color coded by the month in which this change was detected. Although this approach might seem counterintuitive, it is practical since maintenance work on the Portuguese FBN occurs only once a year, usually in the first six months, making it sensible to detect only the first change to bare ground within that year.

3.2 Processing Steps Analysis

The previous section demonstrated the workflow of the proposed methodology by outlining the sequence of steps taken to detect changes related to maintenance work within an

FB. In this section, each step will be explained with more detail. But, first and foremost, it's important to explain what are the two required resources needed before starting preprocessing. The first resource is the Sentinel-1 SAR GRD image collection. The second resource is the FB geometry which can be imported into GEE as an asset. This asset, also called a feature collection, is imported through shapefiles. A shapefile is an Esri vector data storage format, commonly used to store georeferenced features in GIS applications[45]. The Portuguese primary FBN is readily available online and provided by the Institute for Nature Conservation and Forests[46]. Custom shape files for a complete FBN can also be developed in GIS software.

3.2.1 Filter Collection

Filtering the Sentinel-1 SAR collection on GEE is quite simple, and can be achieved by searching for specific parameters. The used parameters in the filtering process are listed bellow.

- **Instrument Mode** - IW.
- **Contains Transmitter Receiver Polarization** - VV and VH.
- **Date** - Start and end date of a given year.
- **Bounds** - FB Geometry

Filtering the bounds of a given feature geometry only ensures the images contain the feature. This alone will not reduce the image size to the area of the geometry itself. To get a smaller image that is easier to work with, a rectangular bounding box is created around the selected FB geometry and then used to crop the image.

3.2.2 Slope Correction

Correcting SAR images for layover and shadow effects is a fundamental step in this methodology. The applied slope correction method was provided by [43].

The process starts with a decibel to power conversion, since SAR images are provided in a decibel scale and radiometric calculations must be done with linear power units (Watt). Equation 3.1 illustrates how this conversion is performed, where I represents the decibel value of the original image.

$$\sigma^0 = 10^{\frac{I}{10}} \tag{3.1}$$

Two types of geometry must be combined to correct the images. The first type is the RADAR geometry, with its main components being the incidence angle θ_i and range angle ϕ_i. GEE only provides the incidence angle in the image metadata, therefore the range angle for a pixel is computed with a gradient of the neighbouring pixels incidence

angles. The other geometry is the terrain geometry. A DEM, more specifically NASA's Shuttle Radar Topography Mission (SRTM) 30m model, provides the required information for terrain geometry, and the obtained angles are the slope steepness ϕ_s and the slope aspect α_s. The interaction between these two geometries is simplified into a single model, described by the slope steepness in range α_r, the incidence angle θ_i, and the signal's strength represented by gamma nought γ^0.

$$\alpha_r = \arctan(\tan(\alpha_s)\cos(\phi_i - \phi_s)) \tag{3.2}$$

$$\gamma^0 = \frac{\sigma^0}{\cos(\theta_i)} \tag{3.3}$$

After computing the model's geometry parameters, a volumetric model[47] described by the equation 3.4 can be applied to flatten the image (angle units are in degrees). The slope correction is concluded with the unit conversion from power to decibels, equation 3.5.

$$\gamma^0_f = \gamma^0 \frac{\tan(90 - \theta_i)}{\tan(90 - \theta_i + \alpha_r)} \tag{3.4}$$

$$\gamma^0_{fdB} = 10\log_{10}(\gamma^0_f) \tag{3.5}$$

The following figures display how the slope correction processing step affects the untreated GRD SAR images. Both Figure 3.3 and Figure 3.4 display how RTC slope correction removes most of the topographic artifacts, making it a fundamental step to distinguish different types of land cover.

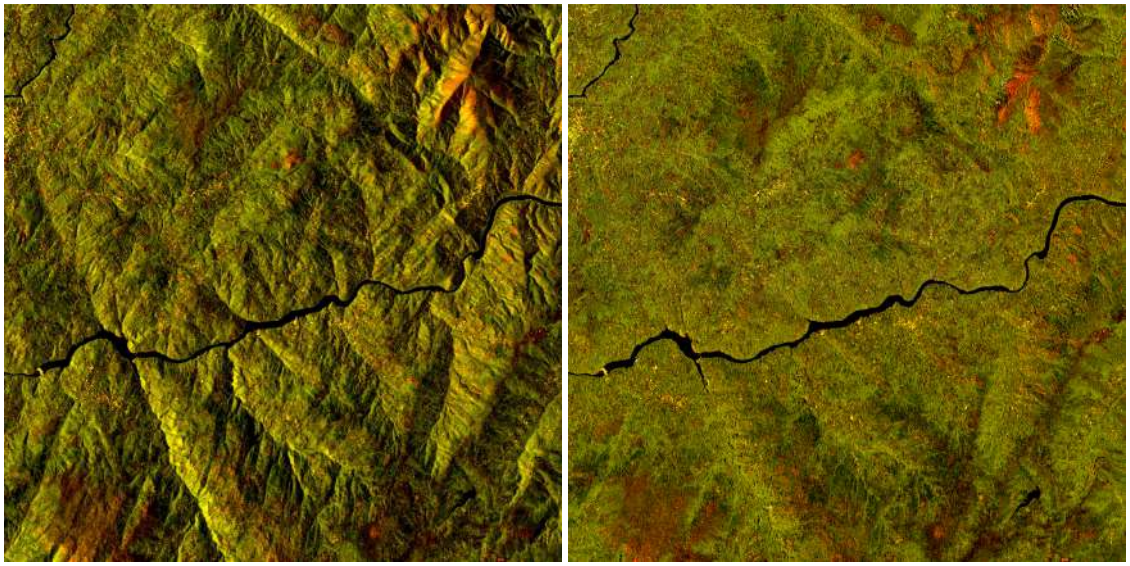

Figure 3.3: SAR composite images of the ascending orbit. Left image without slope correction and right image with slope correction.

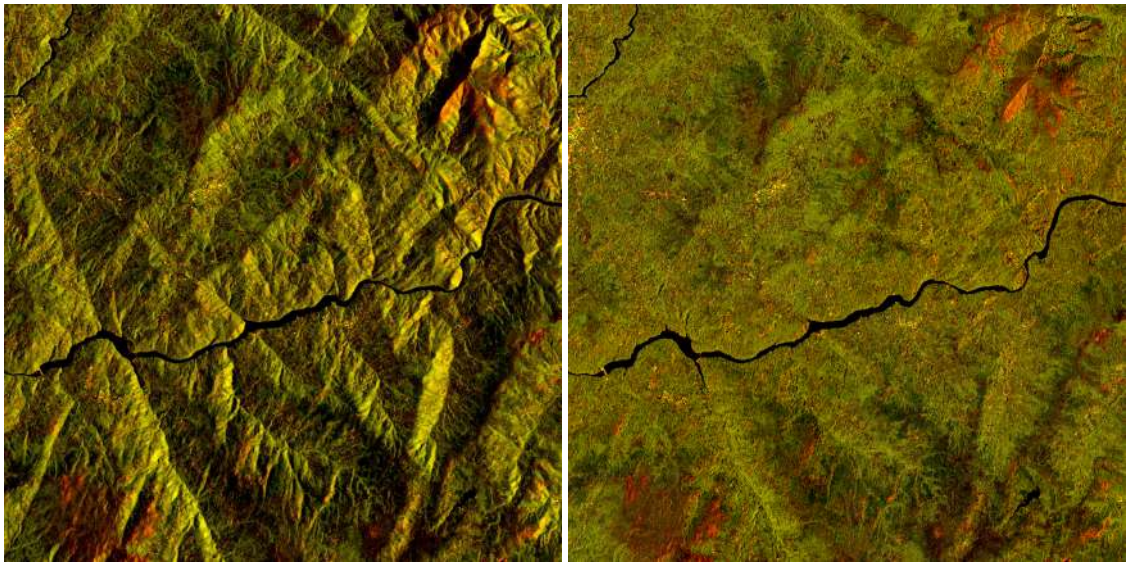

Figure 3.4: SAR composite images of the descending orbit. Left image without slope correction and right image with slope correction.

Another important aspect is orbit direction and the impact it has on images from the same location. By comparing the ascending and descending orbit images without slope correction, it can be seen how layover and shadow regions vary in location depending on orbit direction. On the other side, when images from both ascending and descending orbits are slope corrected they become extremely similar, but not completely. This similarity will enable the use of both orbits to create a single SAR monthly composite.

3.2.3 Refined Lee Filter

Speckle noise in SAR images is another characteristic that needs to be dealt with in order to make the images usable as explained in sections 2.1.5 and 2.2.2.1. The adopted solution to deal with speckle noise is given by [24] and consists of a Refined Lee filter with a kernel size of 7x7.

In similarity with the slope correction, the calculations must be performed with linear scaling units, therefore, the first step is to ensure that the signal values are in the correct Watt power units. This is followed by determining the mean μ and variance σ^2, on a 3x3 window, of each pixel with (x, y) coordinates as seen on equations 3.6 and 3.7.

$$\mu_{3\times3}(x,y) = \frac{1}{9}\sum_{i=-1}^{1}\sum_{j=-1}^{1} I(x+i, y+j) \tag{3.6}$$

$$\sigma^2_{3\times3}(x,y) = \frac{1}{9}\sum_{i=-1}^{1}\sum_{j=-1}^{1} (I(x+i, y+j) - \mu_{3\times3}(x,y))^2 \tag{3.7}$$

The mean and variance values will be sampled from a 7x7 kernel (equation 3.8), where value 1 indicates a sampled value and 0 a non sampled value. In total, nine mean and variance values will be obtain from this step.

$$Sample\ Kernel = \begin{bmatrix} 0 & 0 & 0 & 0 & 0 & 0 & 0 \\ 0 & 1 & 0 & 1 & 0 & 1 & 0 \\ 0 & 0 & 0 & 0 & 0 & 0 & 0 \\ 0 & 1 & 0 & 1 & 0 & 1 & 0 \\ 0 & 0 & 0 & 0 & 0 & 0 & 0 \\ 0 & 1 & 0 & 1 & 0 & 1 & 0 \\ 0 & 0 & 0 & 0 & 0 & 0 & 0 \end{bmatrix} \tag{3.8}$$

With the sampled mean values the next step is determining the four main gradients and the maximum gradient among them. These gradients will mask intermediate calculated values for the directional mean and variance variables.

$$G_1 = |\mu_0 - \mu_8| \quad G_2 = |\mu_1 - \mu_7| \quad G_3 = |\mu_2 - \mu_6| \quad G_4 = |\mu_3 - \mu_5| \tag{3.9}$$

$$G_{max} = \max(G_1, G_2, G_3, G_4) \tag{3.10}$$

Following the gradients, a set of kernels is generated by consecutive 45º rotations of a rectangular kernel and a diagonal kernel, both of which are shown below.

$$K_{rect} = \begin{bmatrix} 0 & 0 & 0 & 0 & 0 & 0 & 0 \\ 0 & 0 & 0 & 0 & 0 & 0 & 0 \\ 0 & 0 & 0 & 0 & 0 & 0 & 0 \\ 1 & 1 & 1 & 1 & 1 & 1 & 1 \\ 1 & 1 & 1 & 1 & 1 & 1 & 1 \\ 1 & 1 & 1 & 1 & 1 & 1 & 1 \\ 1 & 1 & 1 & 1 & 1 & 1 & 1 \end{bmatrix} \quad K_{diag} = \begin{bmatrix} 1 & 0 & 0 & 0 & 0 & 0 & 0 \\ 1 & 1 & 0 & 0 & 0 & 0 & 0 \\ 1 & 1 & 1 & 0 & 0 & 0 & 0 \\ 1 & 1 & 1 & 1 & 0 & 0 & 0 \\ 1 & 1 & 1 & 1 & 1 & 0 & 0 \\ 1 & 1 & 1 & 1 & 1 & 1 & 0 \\ 1 & 1 & 1 & 1 & 1 & 1 & 1 \end{bmatrix} \tag{3.11}$$

Each kernel K, centered at (x, y) coordinates and with a rotational index n, represents a specific direction, and will be used in the equations 3.12 and 3.13 to calculate directional mean and variance values, μ_{dir} and σ^2_{dir} accordingly. According to the masked gradient, only the values calculated with the matching directional kernel will be saved.

$$\mu_{dir}(x, y) = \sum_{n=0}^{4} \frac{\sum_{i=-3}^{3} \sum_{j=-3}^{3} I(x+i, y+j) K_n(i, j)}{\sum_{i=-3}^{3} \sum_{j=-3}^{3} K_n(i, j)} \tag{3.12}$$

$$\sigma^2_{dir}(x, y) = \sum_{n=0}^{4} \frac{\sum_{i=-3}^{3} \sum_{j=-3}^{3} (I(x+i, y+j) - \mu_{dir}(x, y))^2 K_n(i, j)}{\sum_{i=-3}^{3} \sum_{j=-3}^{3} K_n(i, j)} \tag{3.13}$$

Another variable that needs to be calculated is the local variance σ_V. For that, the five lowest sampled mean values are used in conjunction with the respective variance values and averaged with the equation 3.14.

$$\sigma_V = \frac{1}{5} \sum_{i=1}^{5} \frac{\sigma^2_{3\times3\,i}}{\mu^2_{3\times3\,i}} \tag{3.14}$$

With the previously calculated variance values, a variance estimate σ_X^2 can be obtained with equation 3.15.

$$\sigma_X^2 = \frac{\sigma_{dir}^2 - \mu_{dir}^2 \sigma_V}{\sigma_V + 1} \tag{3.15}$$

Before converting back to decibel, the speckle noise present in the image can be finally filtered with the equation 3.16.

$$I_{filtered} = \mu_{dir} + \frac{\sigma_X^2}{\sigma_{dir}^2}(I_{original} - \mu_{dir}) \tag{3.16}$$

This filter can significantly reduce speckle noise, facilitating the detection of features and their respective boundaries in SAR images. The filter's effect can be seen on the following figure, where the processed image holds onto the distinctive features while losing the grainy characteristic seen on the unfiltered image.

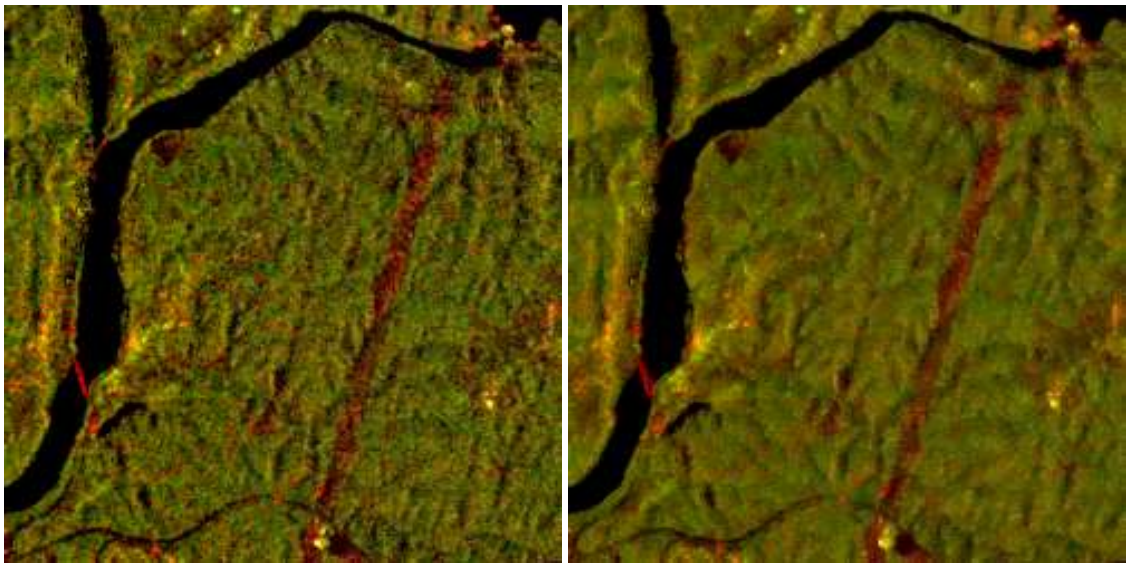

Figure 3.5: Effect of the Refined Lee filter, unfiltered image on the left and filtered image on the right.

3.2.4 Monthly Median

The Sentinel-1 SAR GRD collection includes images with a timestamp indicating the exact date each image was captured. To create the monthly median, images taken within the same month are grouped together, and the median value for each pixel is calculated. The resulting composite image is then assigned a new timestamp, corresponding to the first day of that month.

In this step, no distinction is made between ascending and descending orbits due to the slope correction process. However, monthly orbit bias can still occur. Since the slope correction does not completely eliminate topography-induced distortions, combining

images from different orbits can lead to future issues. For instance, if more images are captured in the descending orbit in one month, the monthly median may be skewed towards it. If the next month has more ascending orbit images, the median shifts in favor of the ascending orbit. This month-to-month variation in orbit bias can negatively affect the methodology, as detected changes might be due to the orbit bias rather than actual changes. Separating each orbit into a different image processing pipeline would be a last resort to combat orbit bias, which is not necessary in this methodology.

3.2.5 Ratio Band

The ratio band is the final step in preprocessing and involves adding a new band to the existing VV, VH, and angle bands. This new band contains ratio values calculated by dividing the VV band by the VH band at each pixel, which will improve land cover classification as described in [48]. The ratio is computed using equation 3.17, where once again (x, y) represents the pixel coordinates.

$$I(x, y, ratio) = \frac{I(x, y, VV)}{I(x, y, VH)} \tag{3.17}$$

3.2.6 Binary Classification

Image binary classification in this methodology is performed using the built-in classification suite in GEE, which includes classifier models and the necessary tools for training and testing.

The classifier selected for this task is Google's implementation of the Classification and Regression Trees (CART) classifier, which will be used to distinguish between two land cover types, bare ground and vegetation, and was chosen since it is widely used for land cover classification applications in GEE. These classes were chosen because the study areas are not expected to contain water bodies or urbanized regions.

Supervised training was used to develop the classifier, which requires a labeled dataset. This dataset was created using monthly composite RGB images from Sentinel-2 to ensure more accurate labeling. Relying solely on processed SAR images could have reduced accuracy, as important features necessary for labeling might only be visible in one image type. Data from the VV, VH and ratio (VV/VH) bands was used to train the classifier with the intent of achieving better classification accuracy, as described in [48].

Class labeling with only two existing classes is simple. Pixels labeled as bare ground receive the value 0 while the value 1 is attributed to vegetation pixels. Figure 3.6a depicts labeled areas of bare ground and vegetation over a Sentinel-2 RGB image. Relevant training data is then retrieved from the respective SAR monthly composite. The inclusion of data from various geographic locations and seasons is an additional and important aspect of the training dataset. This inclusion was done with the goal of creating a robust classifier, capable of reproducing accurate results on unseen locations and regardless of the date in which the images were acquired.

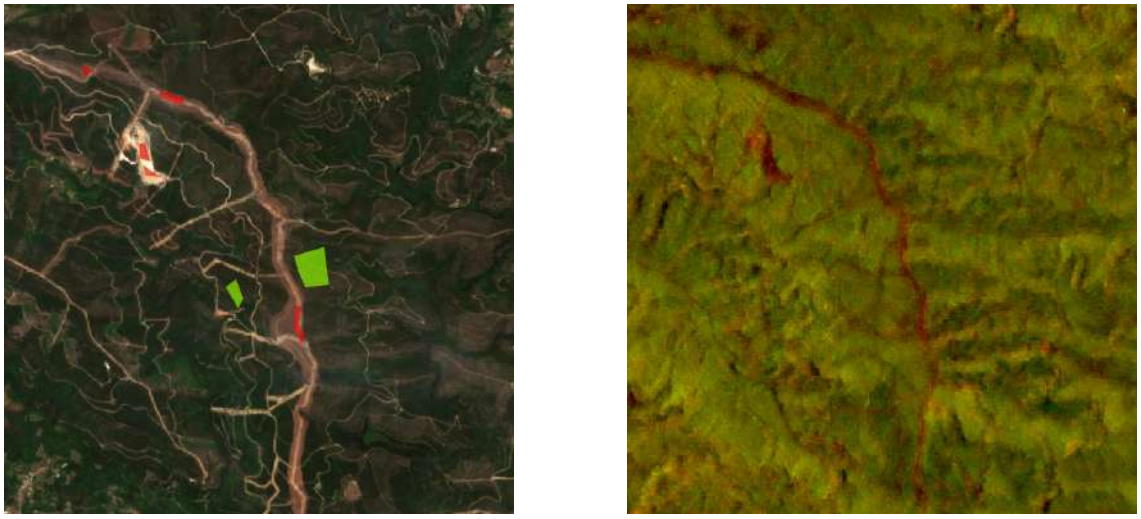

(a) Sentinel-2 RGB June

(b) SAR June

Figure 3.6: Regions labeled bare ground (red) and labeled vegetation (green) over a Sentinel-2 image and respective SAR image, from which data will be extracted.

After creating the labeled dataset, training can be done with the entire labeled dataset (around 15000 labeled pixels). A more detailed explanation about why this is done will be given with the classifier's metrics and evaluation in the next chapter. The binary classified image correspondent to the SAR image in Figure 3.6b can be seen on Figure 3.7. The green region represents pixels classified as vegetation while the brown regions are the pixels classified as being bare ground. At the naked eye it is already possible to notice that the classification done has a high degree of resemblance to what a human would classify as vegetation and bare ground on the Sentinel-2 RGB image.

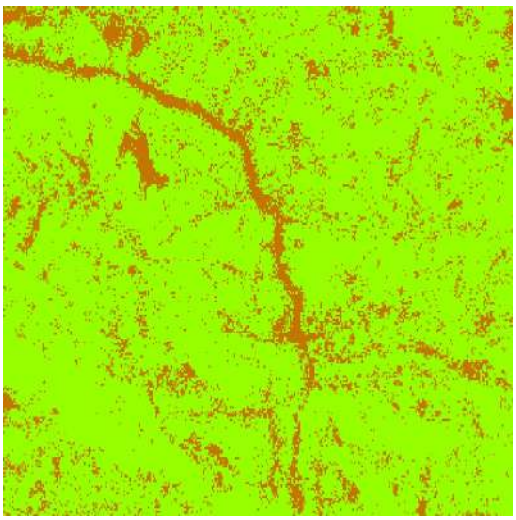

Figure 3.7: June binary classified image.

3.2.7 Difference Image

A difference image can be created with various methods, as described earlier in section 2.2.2.6. Nonetheless, as this step involves classified images with pixels taking values of either 0 or 1, a simple subtraction can be done to create the difference image. Equation 3.18 is used for the creation of the difference image collection, where n represents the month correspondent to each image. Additionally, there is no need to specify the used band in this operation since a classified image is comprised of a single band, in which classes are attributed by giving different values to the pixels.

$$(DI_2, ..., DI_n) = ((I_1 - I_2), ..., (I_{n-1} - I_n)) \tag{3.18}$$

The product of this operation is an image with pixel values ranging from -1 to 1, and each value indicates a type of change.

- **No Change**: 0
- **Change to Bare Ground**: 1
- **Change to Vegetation**: -1

3.2.8 Charting

In order to create a chart, a geometry must be provided and it can be polygon or a point, in this case it should be the geometry of a selected FB. The process of selecting the geometry shape is critical, as only the pixels within it will be used in the analysis methods.

Charting can be divided into two categories, SAR band charting and class charting. The difference between these two categories is given by the chosen approach for displaying the acquired data. In SAR band charting, the selected pixels will be averaged into a single value, resulting in a mean monthly intensity value dataset. However, averaging out pixels with different class values will not result in something with meaningful value for analysis. For this reason, class charting provides a dataset with the occupied area from each class. This dataset is achieved by counting the number of pixels each class has, and to get the correct area values, a value of 20m is given for the dimension of each side of the pixel[21].

3.2.9 Yearly Change Evolution

The yearly change map is generated by identifying the first occurrence of a change to bare ground for each pixel. To do this, the change map collection must be sorted by date, from oldest to most recent. The final change map is created by iterating through this sorted collection and assigning each pixel the index value of its first appearance with a value of 1, indicative of the change to bare ground. This map makes it easy to see when and where maintenance work has occurred.

4

Evaluation Metrics and Results

Validating any methodology requires the support of its results and evaluation metrics. This will be the aim of this chapter and the used method for this purpose will consist of the binary classifier's performance, the change map pixel behavior analysis, and finally, the analysis of the results produced by the developed methodology.

4.1 Evaluation Metrics

The evaluation metrics come from tests carried out on the methodology's geographical transferability and seasonality. Geographic transferability will be a result of how the classifier performs in unseen geographic locations. On the other hand, seasonality will be evaluated by analyzing the behavior of a randomly selected pixel within the collection of change maps generated during the difference image processing step.

4.1.1 Classifier Performance

For the classifier, the chosen metrics were the classifier's accuracy obtained through k-fold cross validation, alongside the f1 score and accuracy acquired by testing the classifier on regions that weren't included in its train dataset. F1 score metrics will be shown with two percentage values stacked vertically, the top value is associated with the bare ground class while the bottom value corresponds to the f1 score given to the vegetation class.

The k-fold cross validation metric, for $k = 5$, is obtained by splitting the train dataset into five subsets, also called as folds. Four folds will be used to train the classifier and the remaining fold will be used to assess the classifier's accuracy. In total, five classifiers will be trained so every fold is used in training and testing. The resulting metric will be the average accuracy obtained by all the trained classifiers.

Accuracy and f1 score are metrics associated to a confusion matrix. The confusion matrix associated to the binary classifier is presented in Table 4.1, with the classifier's accuracy being calculated with equation 4.1.

Table 4.1: Representation of the binary classifier's confusion matrix.

	Predicted Bare Ground	Predicted Vegetation
Actual Bare Ground	True Bare Ground (TBG)	False Vegetation (FV)
Actual Vegetation	False Bare Ground (FBG)	True Vegetation (TV)

$$ACC = \frac{TBG + TV}{TBG + FBG + TV + FV} \tag{4.1}$$

F1 scores, for both bare ground and vegetation classes, are achieved by calculating each class's precision and recall values, and using the f1 score formula with the respective values, as shown bellow.

$$Precision_{BG} = \frac{TBG}{TBG + FBG} \quad Recall_{BG} = \frac{TBG}{TBG + FV} \tag{4.2}$$

$$Precision_{V} = \frac{TV}{TV + FV} \quad Recall_{V} = \frac{TV}{TV + FBG} \tag{4.3}$$

$$F1s = \frac{2 \times Precision \times Recall}{Precision + Recall} \tag{4.4}$$

To evaluate geographic transferability, having a classifier built with a dataset comprised of distinct regions and seasons is a must. The following list shows the chosen regions, alongside month and year, from which data was acquired.

- **Region B** — Boticas, May and June, 2022.
- **Region S** — Seia, August, 2022.
- **Region F** — Figueira da Foz, November, 2022.
- **Region C** — Coimbra, March, 2022.

Tables 4.2, 4.3 and 4.4 display classifier geographic transferability metrics for when the classifier is trained with one, two or three regions accordingly.

Table 4.2: Geographic transferability evaluation metrics for classifiers trained with 1 region.

		Test Regions							
Classifiers		**B**		**S**		**F**		**C**	
Train Regions	5-Fold CVal	F1 Score	ACC	F1 Score	ACC	F1 Score	ACC	F1 Score	ACC
B	99,0%			97,3%	97,8%	97,5%	98,0%	94,7%	95,6%
				98,2%		98,3%		96,2%	
S	93,4%	90,6%	92,6%			90,6%	92,2%	90,5%	91,7%
		93,9%				93,4%		92,7%	
F	98,8%	97,3%	98,2%	94,4%	96,2%			94,1%	95,8%
		98,6%		97,1%				96,7%	
C	95,6%	93,3%	93,6%	95,3%	95,4%	95,1%	95,2		
		93,9%		95,4%		95,3%			

Among the results shown in Table 4.2, there is a clear disparity between the results from Seia and the other regions. When the classifier is trained with a single region, Seia provides the worst transferable classifier while the other regions show similar results, with the exception of the classifier trained with the Coimbra dataset, underperforming in the region of Boticas.

Table 4.3: Geographic transferability evaluation metrics for classifiers trained with 2 regions.

		Test Regions							
Classifiers		**B**		**S**		**F**		**C**	
Train Regions	5-Fold CVal	F1 Score	ACC	F1 Score	ACC	F1 Score	ACC	F1 Score	ACC
B+S	95,8%					95,3% 97,6%	96,8%	95,6% 95,8%	95,7%
B+F	98,8%			91,2% 94,0%	92,9%			94,2% 94,6%	94,4%
B+C	96,6%			91,5% 93,9%	92,9%	96,1% 98,0%	97,3%		
S+F	96,5%	97,6% 98,4%	98,0%					95,8% 95,9%	95,9%
S+C	94,9%	96,0% 97,2%	96,7%			95,0% 97,4%	96,5%		
F+C	97,0%	96,4% 97,5%	97,0%	92,1% 94,2%	93,3%				

Classifiers trained with two regions show a more robust capability of being used in unseen locations, as shown by Table 4.3. Once again, when the Seia dataset isn't included in training, the classifier underperforms in the region, but if present the classifier shows equal performance.

Table 4.4: Geographic transferability evaluation metrics for classifiers trained with 3 regions.

		Test Regions							
Classifiers		**B**		**S**		**F**		**C**	
Train Regions	5-Fold CVal	F1 Score	ACC	F1 Score	ACC	F1 Score	ACC	F1 Score	ACC
B+S+F	97,0%							95,4% 95,5%	95,5%
B+S+C	95,6%					95,8% 97,8%	97,1%		
B+F+C	97,6%			91,9% 94,2%	93,2%				
S+F+C	96,0%	96,8% 97,8%	97,4%						

In Table 4.4 the trend continues, with Seia receiving the lowest accuracy score when

used as the unseen location. Nonetheless, the 5-fold cross validation metric showed consistent accuracy values, above 95%, when Seia was included in the training dataset.

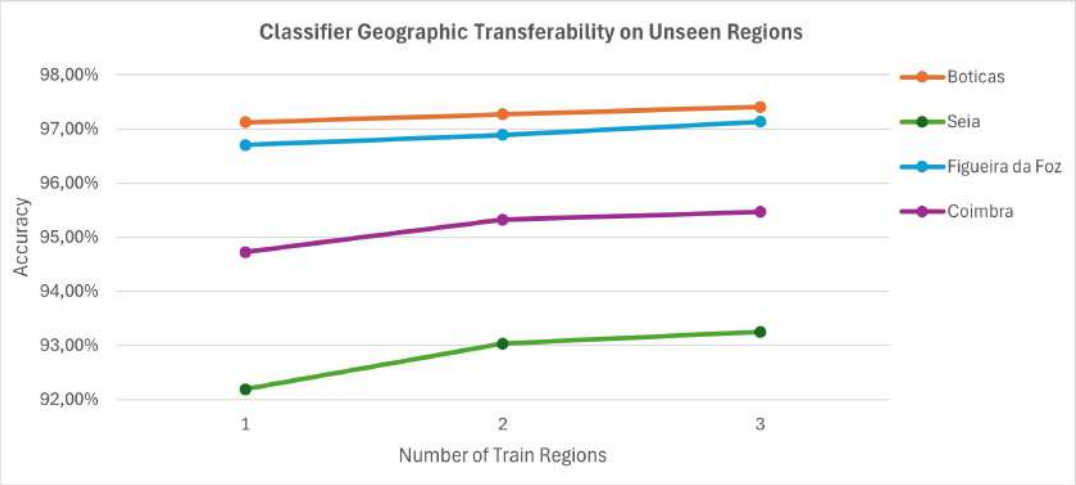

Figure 4.1: Chart of the accuracy evolution on unseen regions according to the number of regions used in training.

From this extensive testing, the observed accuracy values fall in line with what can be seen in other similar approaches for land cover classification such as [48] or [49], where classifier accuracy ranges between 90% and 98%. Figure 4.1 also makes it clear to understand how the number of regions used in the classifier training impact its the performance in unseen regions. The most evident case is Seia, which showed improved performance with each new region added to the training dataset, as the additional data from different regions made the classifier more adaptable to this region.

As result, the direct interpretation of these metrics lead to the decision of building the final classifier using all of the available datasets. The final classifier, used in the developed methodology, had a 96,6% accuracy score in the 5-fold cross validation.

4.1.2 Change Map Pixel Behavior

To test for seasonality, pixel temporal behavior was analyzed by looking at the change map collection generated during the difference image processing step. This analysis involves correlating the changes detected in the pixels with noticeable variations in Sentinel-2 imagery. Three types of behavior were identified: expected, misclassification, and erratic. Since all regions displayed a mix of these behaviors, Boticas was the region selected to exemplify them.

When referring to an expected behavior, a pixel should remain unchanged for most of the year and detect only very relevant changes. Figure 4.2d demonstrates this behavior, where a single change to bare ground is detected from May (Figure 4.2b) to June (Figure 4.2c). While for the remainder of the year, the randomly chosen pixel from the area shown in Figure 4.2a detects no further changes. In the month where changes occurred, 43% of

the area was classified as change to bare ground, while for the rest of the year, an average of 11% of the total area had this label.

(a) FB Area (b) May (c) June

(d) behavior of the randomly chosen pixel from the affected area.

Figure 4.2: Example of an expected behavior for the maintenance work seen on Sentinel-2 imagery.

Misclassification occurs when the change to bare ground is followed by a change to vegetation in the following month. Although not impossible for vegetation to regrow in the span of a month, it is highly improbable when extensive and thorough vegetation removal is done. This can be seen in Figure 4.3e by looking at the months of February and March, where a change to bare ground is detected followed by a change to vegetation. Looking at the following months an an expected behavior can be assumed. The change to bare ground detected in July is also correct, as seen on Sentinel-2 imagery (Figure 4.3). For the selected area, the month where changes occurred saw 53% of the area classified as change to bare ground with the other months averaging 14% for the same label.

The worst case scenario is when a pixel assumes an erratic behavior. Figure 4.4 the maintenance work done in the months of January and February. Although a change to bare ground is being detected in the correct month, the overall behavior of the pixel is erratic. In this case, constant variation in the change detection value occurs, making time series analysis a nonviable option to detect any type of change (Figure 4.4d). Despite the erratic behaviour of this single pixel, 27% of the selected area was classified with a change to bare ground in the month where maintenance work was done, and the rest of the months averaging 6% of the area with change to bare ground detection when none supposedly happened.


(a) FB Area


(b) June


(c) July


(d) August

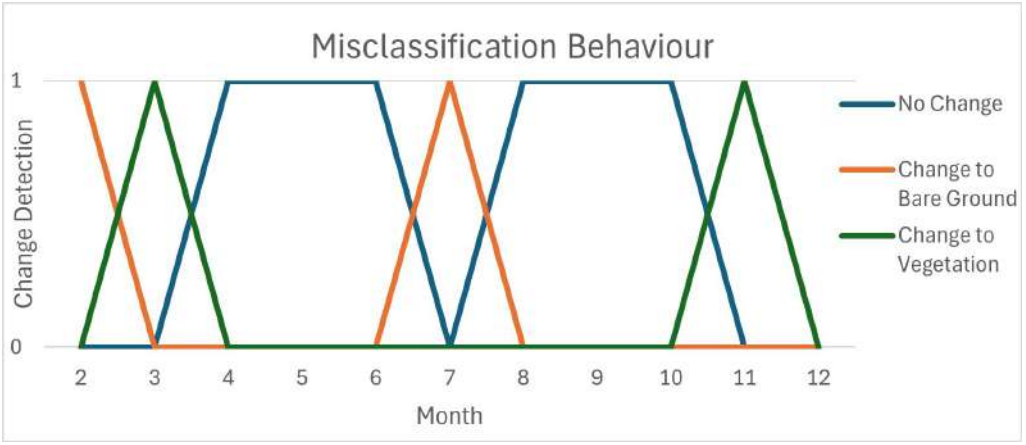

(e) behavior of the randomly chosen pixel from the affected area.

Figure 4.3: Example of a misclassification behavior for the maintenance work seen on Sentinel-2 imagery, where partial cloud coverage is seen in the month where changes occurred.


(a) FB Area


(b) January


(c) February

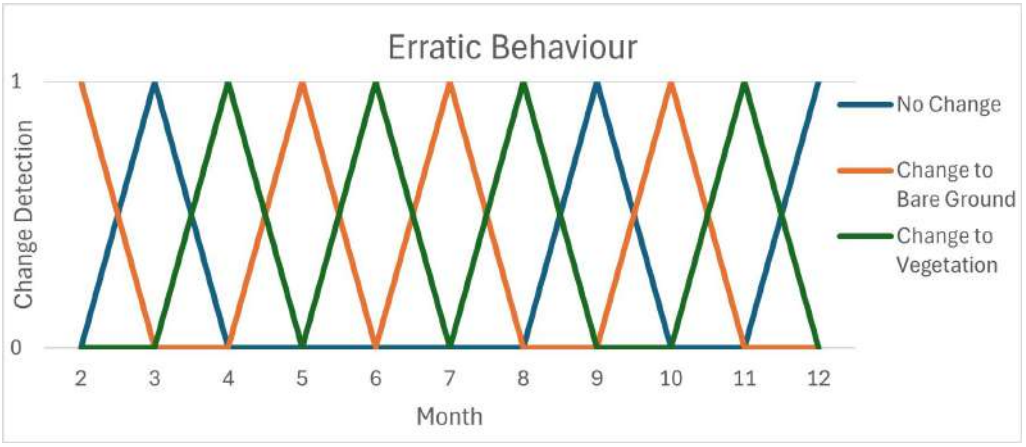

(d) behavior of the randomly chosen pixel from the affected area.

Figure 4.4: Example of an erratic behavior for the maintenance work seen on Sentinel-2 imagery.

Soil moisture, geographic location, orbit bias variation and unforeseen land cover types are all factors that can influence pixel behavior. Misclassification can be said to

be a product of soil moisture and unforeseen land cover, and for this exact reason it can be accounted for by adding a broader range of values and classes to the classification processing step. In the instance of an erratic behaving pixel, the geographic location and orbit bias variation can be assumed to be at the root of the issue. If the pixel is located in a layover or shadow region, the gathered data can be very difficult to process due the vast amount of variables that need to be accounted for and current processing capabilities of GEE's environment.

4.2 Results

The results displayed in this section were obtained by direct application of the proposed image processing methodology. The best and worst performing regions from section 4.1, Boticas and Seia, were selected to provide example results.

CSV file data was lightly processed in Excel to create the presented charts, while the yearly change maps were directly obtained through GEE interface. Additionally, Figure 4.5 serves as support for the correct interpretation of the yearly change maps.

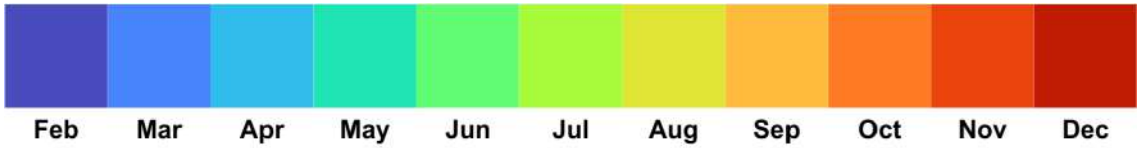

Figure 4.5: Color scale used for the month labeling in yearly change map images.

4.2.1 Boticas

In 2022, a FB was implemented in Boticas during the first half of the year. A portion of this FB can be seen in Figure 4.6a, and its respective yearly change map in Figure 4.6b.

(a) Selected FB

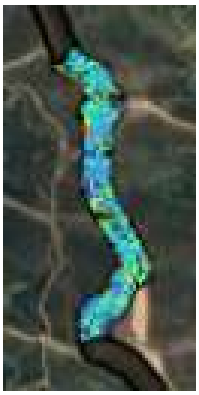

(b) Yearly Change Map

Figure 4.6: Yearly change map for the selected FB.

The change map is mostly comprised of changes detected in the second quarter of the year, an expected result, as this particular section was implemented in the months of

April, May and June.

However, no definite conclusions can be taken from just looking at the yearly change map. To confirm the timing of when changes occurred within the FB, a detailed analysis of the CSV file data is essential. Although possible to extract direct values and metrics from the processed SAR images (Figure 4.7), the real value is in the data acquired from the binary classified images and the monthly change maps.

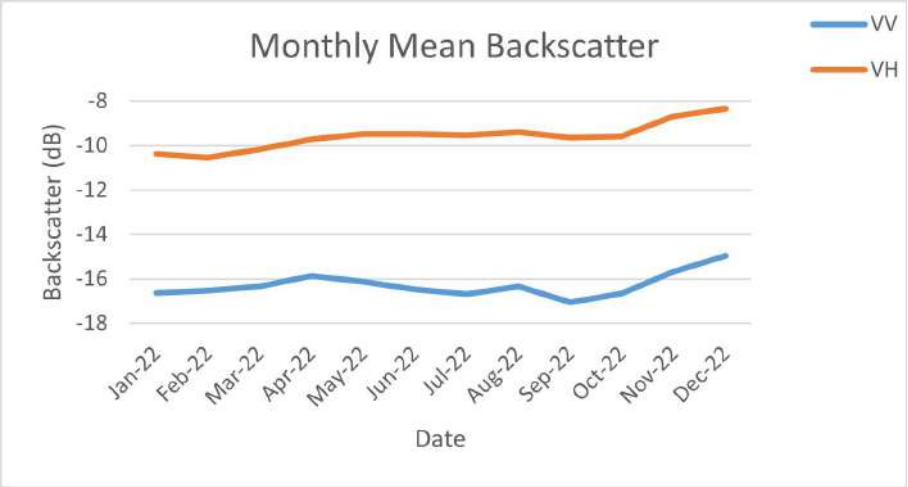

Figure 4.7: Monthly mean VV and VH band values for the selected FB in Boticas.

From the analysis of the monthly land cover area (Figure 4.8), an inverse relationship between bare ground and vegetation area appears. This is explained by the separation of a constant total area between only two types of land cover. In accordance with the timing of the FB implementation, an increase of bare ground area takes place from April to September, with extra relevance being given to the opened gap between the occupied area of each class.

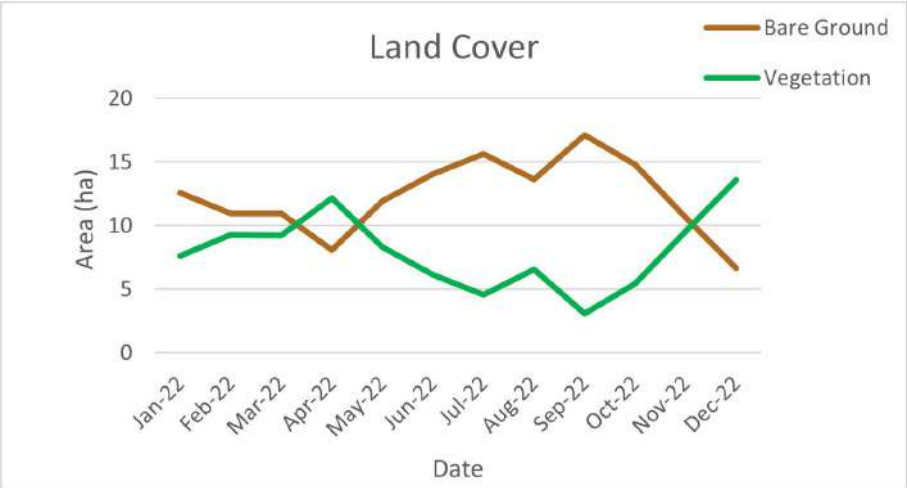

Figure 4.8: Monthly area of each class in the binary image for the selected FB in Boticas.

The last type of chart is derived from the monthly change maps. Maintenance work can

be detected by adding all the pixels labeled with a change to bare ground value followed by applying a threshold to account for the existence of erratic behaving pixels. In Figure 4.9, 25% of the total selected area was used as the threshold value. This value was chosen since the maintenance work done in a month is assumed to occupy more than 25% of the selected area. With this in mind, the resulting chart corroborated the previously acquired information, as in the months of May and June the amount of pixels with the value 1 (change to bare ground value) surpassed the proposed threshold.

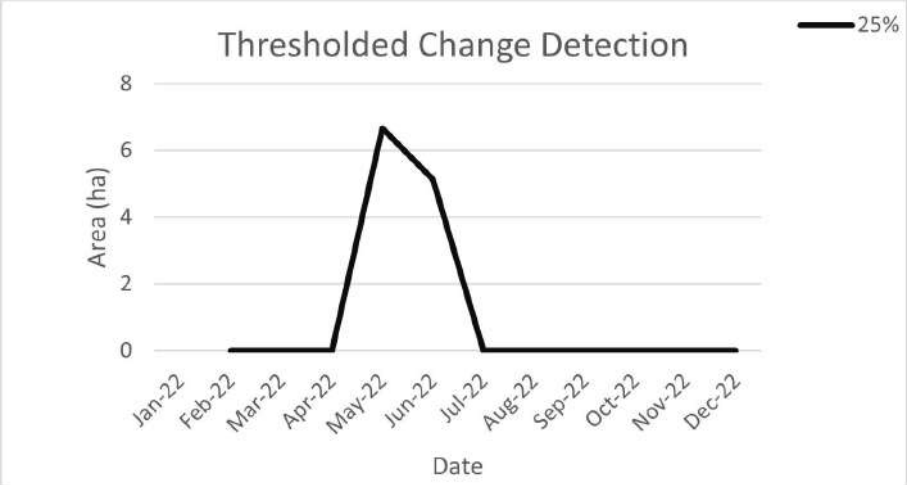

Figure 4.9: Change to bare ground area thresholded at 25% of the total area of the selected FB in Boticas.

To understand how the FB was implemented, the image seen on Figure 4.10 provides further insight on how maintenance work was carried out. Through this change map, it's easy to see the how maintenance work evolved over time, starting from the northwest region (top left of the image) and making its way through to southeast (bottom right of the image).

Figure 4.10: Stitched yearly change maps created from FB sections in Boticas.

4.2.2 Seia

Despite not performing as well as Boticas in the evaluation metrics for the binary classifier, the region of Seia can also benefit from the proposed methodology. Figure 4.11a shows the selected FB from Seia, in which no maintenance work was done in 2022. From a quick glimpse of the yearly change map, it can be seen that the methodology is triggering the detection of a change to bare ground in most of the FB area. Nonetheless, misclassification or erratic behaving pixels can easily disrupt this analysis method, specially taking into account the small dimension of the selected FB.

(a) Selected FB (b) Yearly Change Map

Figure 4.11: Yearly change map for the selected FB.

Once again, through the analysis of the data provided in the CSV files, the true behavior of the FB can be seen. Both bare ground and vegetation areas remained constant throughout the year, with very small fluctuations as seen for example from May to June, as seen in Figure 4.12. This fluctuation can also be directly correlated to the cyan color seen earlier in the yearly change map.

Figure 4.12: Monthly area of each class in the binary image for the selected FB in Seia.

FB area plays a crucial role in determining threshold values. When compared to the selected area from Boticas, the selected area in Seia is one tenth smaller. By using 15% and 10% of the total area values as thresholds, it is possible to test how different

thresholds impact change detection. The results can be seen in Figure 4.13, where the 15% threshold provides an accurate result and the 10% threshold detects the already mentioned fluctuation from May to June. The result provided by the 15% threshold would have been obtained for any superior threshold value, including the previously used 25% threshold.

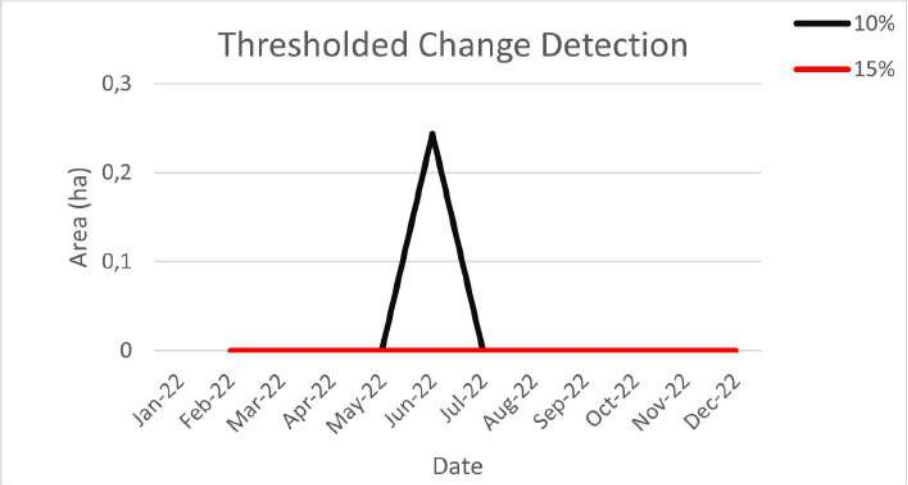

Figure 4.13: Change to bare ground area thresholded at 15% and 10% of the total area of the selected FB in Seia.

FB area is a strict parameter when it comes to analyzing CSV file data. The number of pixels with misclassification and erratic behaviors can scale proportionally with area size. A scaling problem occurs at the point where faulty pixels occupy the usual maintenance work area, surpassing threshold values and making the acquired data unusable.

In summary, the results from both regions demonstrate a high level of accuracy, with all of the available products being essential in determining when maintenance work was performed.

5

Conclusions

To reiterate, this work was driven by the limitations of optical-based methods for detecting maintenance work across Portugal's FBN. To address these limitations, a processing methodology for SAR imagery was proposed. SAR's ability to penetrate cloud cover, unlike optical imagery, was a key factor in choosing this technology. Consequently, this methodology should effectively detect maintenance work within a specified FB area. The SAR data used was sourced from the Sentinel-1A satellite, part of the European Union's Earth observation program named Copernicus.

The data produced with the developed methodology was successfully processed and analyzed, leading to the accurate detection of maintenance work on a designated FB. However, seasonality and geographic location were significant limiting factors, as SAR imagery is highly influenced by these variables. Despite these limitations, the methodology was capable of providing accurate results regardless of location or season when applied to reasonably sized regions.

Nevertheless, the results were obtained in regions from which training data was extract to build the used classifier. A good level of geographic transferability was attributed to the classifier based on the acquired evaluation metrics. However, this could be a potential issue if the classifier was overfitted to its training datatset, making its performance on future unseen regions unknown. Other potential issues with the classifier include errors caused by unaccounted types of land cover and the absence of additional seasonal data in its training. For future improvements, the classifier should be trained on a dataset that includes full seasonal data from all used regions. This could help avoid misclassification in specific areas, such as pixels affected by seasonal flooding. Adding a water class, alongside bare ground and vegetation classes, could also improve accuracy without negatively impacting classifier performance, as land cover classification with more than two classes can achieve acceptable results [50].

Future work will focus on the mitigation of erratic behaving pixels by improving the used classifier, and enhancing existing optical-based change detection methods for FBs by directly utilizing the developed methodology's products. In doing so, this work will achieve its practical goal of aiding forest fire prevention.

Bibliography

[1] J. M. Lourenço. *The NOVAthesis LaTeX Template User's Manual*. NOVA University Lisbon. 2021. URL: https://github.com/joaomlourenco/novathesis/raw/main/template.pdf (cit. on p. i).

[2] D. de Proteção Florestal e Valorização de Áreas Públicas (DPFVAP). *Manual de Rede Primária*. Tech. rep. Instituto da Conservação da Natureza e das Florestas (ICNF), 2014 (cit. on p. 1).

[3] A. Tsokas et al. "SAR data applications in earth observation: An overview". In: *Expert Systems with Applications* 205 (2022), p. 117342. ISSN: 0957-4174. DOI: https://doi.org/10.1016/j.eswa.2022.117342. URL: https://www.sciencedirect.com/science/article/pii/S0957417422006960 (cit. on p. 2).

[4] *Radar Vegetation Index for Sentinel-1 SAR data - RVI4S1 Script*. URL: https://custom-scripts.sentinel-hub.com/custom-scripts/sentinel-1/radar_vegetation_index/ (visited on 2024-11-22) (cit. on p. 2).

[5] *SAR Vegetation Indices*. URL: https://servirglobal.net/sites/default/files/Portals/0/Documents/Articles/2019_SAR_Handbook/SAR_VegIndices_1page_new.pdf (visited on 2024-11-22) (cit. on p. 2).

[6] V. Aubard et al. "Fully Automated Countrywide Monitoring of Fuel Break Maintenance Operations". In: *Remote Sensing* 12.18 (2020). DOI: 10.3390/rs12182879 (cit. on p. 3).

[7] J. E. Pereira-Pires et al. "Pixel-based and object-based change detection methods for assessing fuel break maintenance". In: *2020 International Young Engineers Forum (YEF-ECE)*. 2020. DOI: 10.1109/YEF-ECE49388.2020.9171818 (cit. on p. 3).

[8] F. Meyer. "Spaceborne Synthetic Aperture Radar – Principles, Data Access, and Basic Processing Techniques". In: *The SAR Handbook: Comprehensive Methodologies for Forest Monitoring and Biomass Estimation*. NASA, 2019. DOI: 10.25966/ez4f-mg98 (cit. on pp. 4, 7–11).

[9] W. Fu et al. "Remote Sensing Satellites for Digital Earth". In: *Manual of Digital Earth*. Springer, 2019. DOI: 10.1007/978-981-32-9915-3_3 (cit. on p. 5).

[10] C. A. Wiley. "Synthetic Aperture Radars". In: *IEEE Transactions on Aerospace and Electronic Systems* AES-21.3 (1985), pp. 440–443. DOI: 10.1109/TAES.1985.310578 (cit. on p. 5).

[11] S. D. Jawak, T. G. Bidawe, and A. J. Luis. "A Review on Applications of Imaging Synthetic Aperture Radar with a Special Focus on Cryospheric Studies". In: *Advances in Remote Sensing* 4.2 (2015), pp. 163–175. DOI: 10.4236/ars.2015.42014 (cit. on p. 5).

[12] *Sentiwiki Sentinel-1 S1 Products*. URL: https://sentiwiki.copernicus.eu/web/s1-products (visited on 2024-07-04) (cit. on pp. 5, 10, 11).

[13] T. Fritz and M. Eineder. *TerraSAR-X Ground Segment Basic Product Specification Document*. Tech. rep. German Aerospace Center (DLR), 2013 (cit. on p. 5).

[14] *Introduction to SAR*. URL: https://pro.arcgis.com/en/pro-app/latest/help/analysis/image-analyst/introduction-to-synthetic-aperture-radar.htm (visited on 2024-07-04) (cit. on p. 5).

[15] *Mission Get To Know SAR - Polarimetry*. URL: https://nisar.jpl.nasa.gov/mission/get-to-know-sar/polarimetry/ (visited on 2024-07-04) (cit. on p. 6).

[16] X. Banque et al. "Polarimetry-Based Land Cover Classification with Sentinel-1 Data". In: *POLINSAR 2015, Proceedings of the conference held 26-30 January 2015 in Frascati, Italy*. 2015 (cit. on pp. 7, 13).

[17] M. Arii et al. "Review of the Comprehensive SAR Approach to Identify Scattering Mechanisms of Radar Backscatter from Vegetated Terrain". In: *Electronics* 8 (2019), p. 1098. DOI: 10.3390/electronics8101098 (cit. on p. 8).

[18] S. Zwieback et al. "Depth-Resolved Backscatter and Differential Interferometric Radar Imaging of Soil Moisture Profiles: Observations and Models of Subsurface Volume Scattering". In: *IEEE Journal of Selected Topics in Applied Earth Observations and Remote Sensing* (2017), p. 99. DOI: 10.1109/JSTARS.2017.2671025 (cit. on p. 8).

[19] P. Singh and R. Shree. "Analysis and effects of speckle noise in SAR images". In: *2016 2nd International Conference on Advances in Computing, Communication, Automation (ICACCA) (Fall)*. 2016. DOI: 10.1109/ICACCAF.2016.7748978 (cit. on p. 9).

[20] K. Dasari et al. "Importance of speckle filtering in image classification of SAR data". In: *2015 International Conference on Microwave, Optical and Communication Engineering (ICMOCE)*. 2015. DOI: 10.1109/ICMOCE.2015.7489764 (cit. on p. 9).

[21] *Sentiwiki Sentinel-1 S1 Mission*. URL: https://sentiwiki.copernicus.eu/web/s1-mission (visited on 2024-07-04) (cit. on pp. 10, 31).

[22] A. Lopes, R. Touzi, and E. Nezry. "Adaptive speckle filters and scene heterogeneity". In: *IEEE Transactions on Geoscience and Remote Sensing* 28.6 (1990), pp. 992–1000. DOI: 10.1109/36.62623 (cit. on p. 11).

[23] M. Yahia and T. Ali. "SAR Image Denoising using MMSE Techniques". In: *Denoising*. IntechOpen, 2022. DOI: 10.5772/intechopen.108362 (cit. on p. 11).

[24] A. S. Yommy et al. "SAR Image Despeckling Using Refined Lee Filter". In: *2015 7th International Conference on Intelligent Human-Machine Systems and Cybernetics*. 2015. DOI: 10.1109/IHMSC.2015.236 (cit. on pp. 11, 21, 26).

[25] A. I. Flores-Anderson et al. "Evaluating SAR Radiometric Terrain Correction Products: Analysis-Ready Data for Users". In: *Remote Sensing* 15.21 (2023). DOI: 10.3390/rs15215110 (cit. on p. 11).

[26] M.-H. Ka et al. "A New Single-Pass SAR Interferometry Technique with a Single-Antenna for Terrain Height Measurements". In: *Remote Sensing* 11.9 (2019). DOI: 10.3390/rs11091070 (cit. on p. 12).

[27] *Mission Get To Know SAR - Interferometry*. URL: https://nisar.jpl.nasa.gov/mission/get-to-know-sar/interferometry/ (visited on 2024-07-04) (cit. on p. 12).

[28] A. Orynbaikyzy, U. Gessner, and C. Conrad. "Spatial Transferability of Random Forest Models for Crop Type Classification Using Sentinel-1 and Sentinel-2". In: *Remote Sensing* 14.6 (2022). DOI: 10.3390/rs14061493 (cit. on p. 13).

[29] M. Elsaadouny, J. Barowski, and I. Rolfes. "Unsupervised Learning Implementation for SAR Images Clustering". In: *2021 International Conference on Electromagnetics in Advanced Applications (ICEAA)*. 2021. DOI: 10.1109/ICEAA52647.2021.9539661 (cit. on p. 13).

[30] J. Zhao et al. "Convolutional Neural Network for SAR image classification at patch level". In: *2016 IEEE International Geoscience and Remote Sensing Symposium (IGARSS)*. 2016. DOI: 10.1109/IGARSS.2016.7729239 (cit. on p. 14).

[31] J. Alatalo, T. Sipola, and M. Rantonen. "Improved Difference Images for Change Detection Classifiers in SAR Imagery Using Deep Learning". In: *IEEE Transactions on Geoscience and Remote Sensing* 61 (2023). DOI: 10.1109/TGRS.2023.3324994 (cit. on pp. 14, 16).

[32] *U-Net Architecture Explained*. URL: https://www.geeksforgeeks.org/u-net-architecture-explained/ (visited on 2024-11-24) (cit. on p. 14).

[33] L. Li, H. Ma, and Z. Jia. "Change Detection from SAR Images Based on Convolutional Neural Networks Guided by Saliency Enhancement". In: *Remote Sensing* 13.18 (2021). DOI: 10.3390/rs13183697 (cit. on p. 15).

[34] J. Geng et al. "Change detection of SAR images based on supervised contractive autoencoders and fuzzy clustering". In: *2017 International Workshop on Remote Sensing with Intelligent Processing (RSIP)*. 2017. DOI: 10.1109/RSIP.2017.7958819 (cit. on p. 15).

[35] M. Gong et al. "SAR change detection based on intensity and texture changes". In: *ISPRS Journal of Photogrammetry and Remote Sensing* 93 (2014). DOI: 10.1016/j.isprsjprs.2014.04.010 (cit. on p. 16).

[36] K. Zhang et al. "Unsupervised SAR Image Change Detection Based on Histogram Fitting Error Minimization and Convolutional Neural Network". In: *Remote Sensing* 15.2 (2023). DOI: 10.3390/rs15020470 (cit. on p. 16).

[37] S. Kobayashi and H. Ide. "Rice Crop Monitoring Using Sentinel-1 SAR Data: A Case Study in Saku, Japan". In: *Remote Sensing* 14.14 (2022). DOI: 10.3390/rs14143254 (cit. on p. 17).

[38] K. C. Kornelsen and P. Coulibaly. "Advances in soil moisture retrieval from synthetic aperture radar and hydrological applications". In: *Journal of Hydrology* 476 (2013), pp. 460–489. DOI: 10.1016/j.jhydrol.2012.10.044 (cit. on p. 17).

[39] A. Veloso et al. "Understanding the temporal behavior of crops using Sentinel-1 and Sentinel-2-like data for agricultural applications". In: *Remote Sensing of Environment* 199 (2017), pp. 415–426. DOI: 10.1016/j.rse.2017.07.015 (cit. on p. 17).

[40] J. Kellndorfer. "Using SAR Data for Mapping Deforestation and Forest Degradation". In: *The SAR Handbook: Comprehensive Methodologies for Forest Monitoring and Biomass Estimation*. NASA, 2019. DOI: 10.25966/68c9-gw82 (cit. on p. 18).

[41] *Sentinel-1 SAR GRD: C-band Synthetic Aperture Radar Ground Range Detected, log scaling*. URL: https://developers.google.com/earth-engine/datasets/catalog/COPERNICUS_S1_GRD (visited on 2024-07-27) (cit. on p. 19).

[42] *GEE-S1-GRD-FuelBreak-Monitor*. URL: https://github.com/SimaoVen/GEE-S1-GRD-FuelBreak-Monitor (visited on 2024-11-28) (cit. on p. 21).

[43] A. Vollrath, A. Mullissa, and J. Reiche. "Angular-Based Radiometric Slope Correction for Sentinel-1 on Google Earth Engine". In: *Remote Sensing* 12.11 (2020). DOI: 10.3390/rs12111867 (cit. on pp. 21, 24).

[44] D. H. Hoekman and J. Reiche. "Multi-model radiometric slope correction of SAR images of complex terrain using a two-stage semi-empirical approach". In: *Remote Sensing of Environment* 156 (2015). DOI: 10.1016/j.rse.2014.08.037 (cit. on p. 21).

[45] *Shapefiles*. URL: https://doc.arcgis.com/en/arcgis-online/reference/shapefiles.htm (visited on 2024-08-06) (cit. on p. 24).

[46] *Geovisualizador da RPFGC*. URL: https://geocatalogo.icnf.pt/geovisualizador/rpfgc/ (visited on 2024-09-03) (cit. on p. 24).

[47] D. H. Hoekman. *Radar remote sensing data for applications in forestry*. Wageningen University and Research, 1990 (cit. on p. 25).

[48] S. Abdikan et al. "Land Cover Mapping Using Sentinel-1 SAR Data". In: *The International Archives of the Photogrammetry, Remote Sensing and Spatial Information Sciences* XLI-B7 (2016). DOI: 10.5194/isprs-archives-XLI-B7-757-2016 (cit. on pp. 29, 35).

[49] H. Wang et al. "Land Cover Classification for Polarimetric SAR Images Based on Vision Transformer". In: *Remote Sensing* 14 (2022). DOI: 10.3390/rs14184656 (cit. on p. 35).

[50] S. Fukuda and H. Hirosawa. "Support vector machine classification of land cover: application to polarimetric SAR data". In: *IGARSS 2001. Scanning the Present and Resolving the Future. Proceedings. IEEE 2001 International Geoscience and Remote Sensing Symposium (Cat. No.01CH37217)*. 2001. DOI: 10.1109/IGARSS.2001.976097 (cit. on p. 43).

2024

Vegetation Change Detection using Synthetic Aperture Radar Images: Monitoring Fuel Breaks through SAR Imaging with Sentinel-1

Simão Vendeirinho

NOVA
NOVA SCHOOL OF
SCIENCE & TECHNOLOGY